

# Potential description of charmonium and charmed-strange mesons from lattice QCD

Taichi Kawanai<sup>1\*</sup> and Shoichi Sasaki<sup>2,3†</sup>

<sup>1</sup>*Jülich Supercomputing Center, Jülich D-52425, Germany*

<sup>2</sup>*Department of Physics, Tohoku University, Sendai 980-8578, Japan and*

<sup>3</sup>*Theoretical Research Division, Nishina Center, RIKEN, Wako 351-0198, Japan*

(Dated: October 21, 2018)

We present spin-independent and spin-spin interquark potentials for the charmonium and charmed-strange mesons, which are calculated in 2+1 flavor lattice QCD simulations using the PACS-CS gauge configurations generated at the lightest pion mass ( $M_\pi \approx 156(7)$  MeV) with a lattice cutoff of  $a^{-1} \approx 2.2$  GeV and a spatial volume of  $(3 \text{ fm})^3$ . For the charm quark, we use a relativistic heavy quark (RHQ) action with fine tuned RHQ parameters, which closely reproduce both the experimental spin-averaged mass and hyper-fine splitting of the  $1S$  charmonium. The interquark potential and the quark kinetic mass, both of which are key ingredients within the potential description of heavy-heavy and heavy-light mesons, are determined from the equal-time Bethe-Salpeter (BS) amplitude. The charmonium potentials are obtained from the BS wave function of  $1S$  charmonia ( $\eta_c$  and  $J/\psi$  mesons), while the charmed-strange potential are calculated from the  $D_s$  and  $D_s^*$  heavy-light mesons. We then use resulting potentials and quark masses as purely theoretical inputs so as to solve the nonrelativistic Schrödinger equation for calculating accessible energy levels of charmonium and charmed-strange mesons without unknown parameters. The resultant spectra below the  $D\bar{D}$  and  $DK$  thresholds excellently agree with well-established experimental data.

## I. INTRODUCTION

The heavy-quark ( $Q$ )-antiquark ( $\bar{Q}$ ) potential is an important quantity to understand properties of the heavy quarkonium states. Because the dynamics of heavy quarks with masses much larger than the QCD scale ( $\Lambda_{\text{QCD}}$ ) is well described within the framework of nonrelativistic quantum mechanics [1]. Indeed the constituent quark potential models with a QCD-motivated  $Q\bar{Q}$  potential have successfully predicted the heavy quarkonium spectra and its decay rates below open charm thresholds [2–4].

In such nonrelativistic potential (NRp) models, the conventional heavy quarkonium states such as charmonium and bottomonium are well understood to be quark-antiquark pair bound by the Coulombic potential induced by a perturbative one-gluon exchange that dominates in short range, plus linearly rising potential that describes the phenomenology of confining quark interactions at large distances [2]. This potential is called the Cornell potential and its functional form is given by

$$V(r) = -\frac{4}{3} \frac{\alpha_s}{r} + \sigma r + V_0 \quad (1)$$

where  $\alpha_s$  is the strong coupling constant,  $\sigma$  denotes the string tension and  $V_0$  is the constant term associated with a self-energy contribution of the color sources. In addition to the spin-independent potential, the NRp models include spin-dependent interactions, which resolve the degeneracy among spin-multiplets. The spin-dependent potentials appear as relativistic corrections in powers of

the relative velocity of quarks, and their functional forms are also determined by perturbative one-gluon exchange as the Fermi-Breit type potential [5]. A more direct connection to QCD is established by the modern approach of effective field theory called potential nonrelativistic QCD (pNRQCD) [6].

We would like to stress here that the functional forms of the  $Q\bar{Q}$  potentials except at long distances are basically deduced by the perturbative approach. Furthermore all of parameters needed in the NRp models, including a constituent quark mass  $m_Q$ , are phenomenologically fixed to reproduce the experimental heavy quarkonium masses [3, 4]. The phenomenological spin-dependent potentials based on the perturbative method would have validity only at short distances and also in the vicinity of the heavy quark mass limit. This fact could cause large uncertainties in predictions for the higher-lying states of the heavy quarkonium in the NRp models.

In addition, many of the charmonium-like mesons have been announced by  $B$ -factories at KEK and SLAC, which are primarily devoted to the physics of CP violation, also by Charm factories at BEPC and CESR, and Tevatron at Fermilab. These newly discovered state above the open charm threshold could not be simply explained as conventional charmonium states in the constituent quark description [7]. Indeed, the existence of the charged  $Z$  states including two charged bottomonium-like states,  $Z_b(10610)$  and  $Z_b(10650)$  [8] indicates that the charmonium-like  $XYZ$  mesons are good candidates for non-standard quarkonium mesons such as hadronic molecular states, diquark-antidiquark bound states (tetraquark states), or hybrid mesons [9].

To discriminate between standard and nonstandard mesons in a zoo of the charmonium-like  $XYZ$  mesons, it is essential to investigate the validity of the potential

\*Electronic address: [t.kawanai@fz-juelich.de](mailto:t.kawanai@fz-juelich.de)

†Electronic address: [ssasaki@nucl.phys.tohoku.ac.jp](mailto:ssasaki@nucl.phys.tohoku.ac.jp)

description of the heavy-heavy and heavy-light mesons directly from first principles of QCD. In this paper, we thus aim to provide the central  $Q\bar{Q}$  potentials (the spin-independent potential and the spin-spin potential), which are determined through the Bethe-Salpeter (BS) amplitudes of pseudoscalar and vector mesons in dynamical lattice QCD simulations with almost physical quark masses.

In lattice QCD, understanding the properties of  $Q\bar{Q}$  interactions is one of the great historic milestones. The Wilson loop has been originally introduced as a non-local order parameter in  $Z_2$  gauge theory by Wegner [10]. Subsequently, Wilson generalized it with continuous gauge groups and related it to the static potential between infinitely heavy-quark and antiquark in QCD so as to prove the quark confinement in the strong coupling limit [11]. The static  $Q\bar{Q}$  potential determined from Wilson loops have been precisely determined by lattice QCD in the past decades. The lattice QCD calculations within the Wilson loop formalism support a shape of the Cornell potential [12].

On the other hand, the spin-dependent  $Q\bar{Q}$  potentials regarded as the relativistic corrections to the static potential can be determined within the framework of pNRQCD. Although earlier quenched studies [13, 14] and full QCD studies [15, 16] did not enable us to determine the functional forms of the spin-dependent terms due to large statistical errors, a full set of the spin-dependent terms (*i.e.* spin-spin, spin-orbit and tensor terms) have been successfully calculated in *quenched* QCD with high accuracy by using the multilevel algorithm [17, 18].

It is worth mentioning that the multilevel algorithm employed in Refs. [17, 18] is not easy to be implemented in dynamical lattice QCD simulations. Furthermore, the leading spin-spin potential determined at  $\mathcal{O}(1/m_Q^2)$  in quenched QCD gives an attractive interaction for the higher spin states in the hyperfine multiplet [17, 18]. This contradicts with the spin-spin term of the Fermi-Breit type potential, which is described by a *repulsive* contact interaction. Although one might think that the inverse of the charm quark mass would be far outside the validity region of the  $1/m_Q$  expansion, this issue still remains even at the bottom quark mass.

We develop the new method proposed in our previous works [19–21] in order to obtain *proper interquark potentials at finite quark masses*, which are indispensable for the potential description of the charmonium and charmed-strange mesons. The interquark potential and the quark kinetic mass, both of which are key ingredients within the potential description, can be defined by the equal-time and Coulomb gauge BS amplitude through an effective Schrödinger equation [19]. This new method enables us to determine the interquark potentials including spin-dependent terms at finite quark masses from first principles of QCD, and then fix all parameters needed in the NRp models. In our previous works with quenched lattice simulations [19, 21], we demonstrated that both spin-independent central potential and spin-spin poten-

tial calculated in the BS amplitude method reproduce known results calculated within the Wilson loop formalism in the  $m_Q \rightarrow \infty$  limit. We read off from our  $Q\bar{Q}$  potentials, which may encode all orders of the  $1/m_Q$  expansion, that the  $1/m_Q$  expansion scheme may have the convergence behavior up to the bottom sector, while the charm sector is far outside the validity region for this expansion [21]. Furthermore, we found that the higher order corrections beyond the next-to-leading order are inevitably required for the repulsive feature of the total spin-spin potential even at the bottom sector [21]. In addition, there is no restriction to extend the new method to dynamical calculation [20]. Hereafter we call the new method as *BS amplitude method*.

Once one gets the reliable  $Q\bar{Q}$  potentials, which contain both the spin-dependent contributions as well as the spin-independent central one, we can easily verify how well the potential description is satisfied in the heavy-heavy and heavy-light meson systems through solving the nonrelativistic Schrödinger equation with purely theoretical inputs. If the potential description is valid, many physical observables such as mass spectrum of heavy-heavy and heavy-light mesons and their decay rates are easily accessible as is in the NRp models.

In this paper, we extend our previous work [20] done in 2+1 flavor lattice QCD simulations using the PACS-CS gauge configurations [22] in order to investigate the validity of the potential description of the heavy-heavy and heavy-light mesons. The simulated pion mass ( $M_\pi \approx 156(7)$  MeV) is close to the physical point, while the simulated  $K$  meson mass as  $M_K \approx 554(2)$  MeV is about 10% heavier than the physical value. Although the strange quark is slightly off the physical point, the parameters of clover fermions for the strange quark are chosen to be equal to those of the strange sea quarks used in gauge field generation. For the charm quark, we employ the relativistic heavy quark (RHQ) action that can control large discretization errors induced by large quark mass [23]. The RHQ parameters in the action were calibrated to reproduce the experimental spin-averaged mass and hyperfine splitting of the  $1S$  charmonium.

We first concentrate on the heavy-heavy systems so as to calculate the charm quark mass and the charmonium potential from the BS amplitudes of  $1S$  charmonia ( $\eta_c$  and  $J/\psi$  mesons). We reuse the data, which were previously published in Ref. [20], and then perform a more elaborate analysis proposed in Ref. [21]. New analysis significantly reduces systematic uncertainties on the shape of the charmonium potential at short distances due to the usage of the highly improved Laplacian operator<sup>1</sup>. Once the charmonium potential and the charm quark mass are precisely determined, we can numerically

---

<sup>1</sup> Note that the binding energy of the low-lying charmonium states, which we may consider to be nearly Coulombic bound states, are very sensitive to details of the short-range interaction.

solve the nonrelativistic Schrödinger equation with such theoretical inputs and without additional parameters.

We then extend our research to the  $D_s$  heavy-light meson systems to extract the strange quark mass and the charmed-strange potential from the BS amplitudes of two lightest charmed-strange mesons (*i.e.* the  $D_s$  and  $D_s^*$  heavy-light mesons). We will then discuss the validity of the potential description on both charmonium and charmed-strange mesons.

This paper is organized as follows. In Sec. II, we briefly describe the methodology to calculate the spin-independent and spin-dependent interquark potentials from the BS amplitude of heavy-heavy and heavy-light mesons in lattice QCD simulations. In Sec. III we give the details of parameters used in our Monte Carlo simulations, and then discuss the charmonium mass obtained from the standard lattice spectroscopy with two point correlation functions of mesons. In Sec. IV, we show numerical results of the BS wave function, the quark kinetic mass  $m_Q$ , the spin-independent central and spin-spin potentials, calculated from dynamical lattice QCD simulations. In Sec. V, we show the charmonium mass spectrum obtained by solving the nonrelativistic Schrödinger equation with the theoretical inputs determined from dynamical lattice QCD simulations at almost physical point, and finally discuss possible systematic uncertainties on the resulting energy spectrum of the charmonium states. In Sec. VI, we present the results from an application to the  $D_s$  heavy-light meson systems. In Sec. VII, we summarize and discuss all results and future perspectives.

## II. FORMALISM

In this section, we will briefly review the BS amplitude method to calculate the interquark potential with the finite quark mass. This is an application based on the approach originally used for the hadron-hadron potential, which is defined through the equal-time BS amplitude [24–33]. More details of determination of the interquark potential are given in Ref. [21].

For simplicity, we here consider the case of the heavy quarkonium  $Q\bar{Q}$ . An extension to the heavy-light meson made of two non-degenerate quarks is easy. In lattice simulations, we measure the following equal-time  $Q\bar{Q}$  BS amplitude in the Coulomb gauge for the quarkonium states [34, 35]:

$$\phi_\Gamma(\mathbf{r}) = \sum_{\mathbf{x}} \langle 0 | \bar{Q}(\mathbf{x}) \Gamma Q(\mathbf{x} + \mathbf{r}) | Q\bar{Q}; J^{PC} \rangle, \quad (2)$$

where  $\mathbf{r}$  is the relative coordinate between quark and antiquark at a certain time slice  $t$ . The operator  $\Gamma$  appeared in Eq. (2) represents the Dirac  $\gamma$  metrics, which specifies the spin and the parity of meson operators. For instance, with  $\gamma_5$  and  $\gamma_i$ , one can form the pseudoscalar (PS) and the vector (V) operators with  $J^P = 0^-$  and  $J^P = 1^-$ , respectively. A summation over spatial coordinates  $\mathbf{x}$  projects out corresponding states with zero

total momentum. The  $\mathbf{r}$ -dependent amplitude,  $\phi_\Gamma(\mathbf{r})$ , is called *BS wave function*. The BS wave function can be extracted from the four-point correlation function

$$G_\Gamma(\mathbf{r}, t, t_s) = \sum_{\mathbf{x}, \mathbf{x}', \mathbf{y}'} \langle 0 | \bar{Q}(\mathbf{x}, t) \Gamma Q(\mathbf{x} + \mathbf{r}, t) \times (\bar{Q}(\mathbf{x}', t_s) \Gamma Q(\mathbf{y}', t_s))^\dagger | 0 \rangle \quad (3)$$

at large time separation between the source ( $t_s$ ) and sink ( $t$ ) locations ( $|t - t_s|/a \gg 1$ ) [21]. Here, the gauge field configurations are necessarily fixed to the Coulomb gauge at both time slices  $t$  and  $t_s$ . In the limit of  $\mathbf{r} \rightarrow 0$ , the four-point correlation functions are reduced to the two-point correlation functions of mesons with a wall source. In this paper, we focus only on the  $S$ -wave BS wave function ( $\eta_c$  and  $J/\psi$  for the charmonium and  $D_s$  and  $D_s^*$  for the charmed-strange meson), obtained by an appropriate projection to the  $A_1^+$  representation in cubic group [36].

Below the inelastic threshold <sup>2</sup>, the BS wave function satisfies an effective Schrödinger equation with a nonlocal and energy-independent interquark potential  $U$  [24, 37, 38]

$$-\frac{\nabla^2}{2\mu} \phi_\Gamma(\mathbf{r}) + \int dr' U(\mathbf{r}, \mathbf{r}') \phi_\Gamma(\mathbf{r}') = E_\Gamma \phi_\Gamma(\mathbf{r}), \quad (4)$$

where  $\mu$  is the reduced mass of the  $Q\bar{Q}$  system. The energy eigenvalue  $E_\Gamma$  of the stationary Schrödinger equation is supposed to be  $M_\Gamma - 2m_Q$ . If the relative quark velocity  $v = |\nabla/m_Q|$  is small as  $v \ll 1$ , the nonlocal potential  $U$  can generally expand in terms of the velocity  $v$  as  $U(\mathbf{r}', \mathbf{r}) = \{V(r) + V_S(r) \mathbf{S}_Q \cdot \mathbf{S}_{\bar{Q}} + V_T(r) S_{12} + V_{LS}(r) \mathbf{L} \cdot \mathbf{S} + \mathcal{O}(v^2)\} \delta(\mathbf{r}' - \mathbf{r})$  where  $S_{12} = (\mathbf{S}_Q \cdot \hat{\mathbf{r}})(\mathbf{S}_{\bar{Q}} \cdot \hat{\mathbf{r}}) - \mathbf{S}_Q \cdot \mathbf{S}_{\bar{Q}}/3$  with  $\hat{\mathbf{r}} = \mathbf{r}/r$ ,  $\mathbf{S} = \mathbf{S}_Q + \mathbf{S}_{\bar{Q}}$  and  $\mathbf{L} = \mathbf{r} \times (-i\nabla)$  [24]. Here,  $V$ ,  $V_S$ ,  $V_T$  and  $V_{LS}$  represent the spin-independent central, spin-spin, tensor and spin-orbit potentials, respectively.

The Schrödinger equation for  $S$ -wave states is simplified as

$$\left\{ -\frac{\nabla^2}{m_Q} + V(r) + \mathbf{S}_Q \cdot \mathbf{S}_{\bar{Q}} V_S(r) \right\} \phi_\Gamma(r) = E_\Gamma \phi_\Gamma(r) \quad (5)$$

at the leading order of the  $v$ -expansion. Here, we essentially follow the NRp models, where the  $J/\psi$  state is purely composed of the  $1S$  wave function. However, within this method, this assumption can be verified by evaluating the size of a mixing between  $1S$  and  $1D$  wave functions in principle.

The spin operator  $\mathbf{S}_Q \cdot \mathbf{S}_{\bar{Q}}$  can be easily replaced by its expectation values:  $-3/4$  and  $1/4$  for the PS and V channels, respectively. Then, the spin-independent and

<sup>2</sup> For the charmonium system, the inelastic threshold implies the  $D\bar{D}$  threshold, while the  $DK$  threshold is a counterpart in the charmed-strange meson system.

spin-spin  $Q\bar{Q}$  potentials can be evaluated through the following linear combinations of Eq.(5):

$$V(r) = E_{ave} + \frac{1}{m_Q} \left\{ \frac{3}{4} \frac{\nabla^2 \phi_V(r)}{\phi_V(r)} + \frac{1}{4} \frac{\nabla^2 \phi_{PS}(r)}{\phi_{PS}(r)} \right\} \quad (6)$$

$$V_S(r) = E_{hyp} + \frac{1}{m_Q} \left\{ \frac{\nabla^2 \phi_V(r)}{\phi_V(r)} - \frac{\nabla^2 \phi_{PS}(r)}{\phi_{PS}(r)} \right\}, \quad (7)$$

where  $E_{ave} = M_{ave} - 2m_Q$  and  $E_{hyp} = M_V - M_{PS}$ . The mass  $M_{ave}$  denotes the spin-averaged mass as  $\frac{1}{4}M_{PS} + \frac{3}{4}M_V$ . The derivative  $\nabla^2$  is defined by the discrete Laplacian on the lattice.

In the BS amplitude method, there is a room for optimizing the differential operator since the discrete Laplacian is itself build in the definition of the interquark potential. In Ref. [21], we showed that the discrete Laplacian operator defined in the discrete polar coordinates called *r-Laplacian* is more suitable than the naive one defined in the Cartesian coordinates from the viewpoint of the reduction of the discretization artifacts on the short-range behavior of the interquark potential. The latter was adopted in our earlier works [19, 20], while we use the *r-Laplacian* throughout this paper. For details of the discrete Laplacian operators, we will explain in Sec. IV.

The quark kinetic mass is also an important quantity in the determination of the interquark potentials since Eq. (6) and Eq. (7) requires information of the quark kinetic mass  $m_Q$ . In Ref. [19], we propose to calculate the quark kinetic mass through the large-distance behavior of the difference of “quantum kinetic energies” (the second derivative of the BS wave function normalized by the BS wave function) between the spin-singlet and -triplet states in the hyperfine multiplet. The most simple choice is of course a pair of  $^1S_0$  and  $^3S_1$  states. Contributions of the long-range confining force are canceled out in the difference of “quantum kinetic energies”. Under a simple, but reasonable assumption as  $\lim_{r \rightarrow \infty} V_S(r) = 0$  which implies there is no long-range correlation and no irrelevant constant term in the spin-spin potential, one may expect that the difference of “quantum kinetic energies” at long distances stems only from the hyperfine splitting energy  $E_{hyp}$ . Therefore, the quark kinetic mass can be read off in the following way:

$$m_Q = \lim_{r \rightarrow \infty} \frac{-1}{E_{hyp}} \left\{ \frac{\nabla^2 \phi_V(r)}{\phi_V(r)} - \frac{\nabla^2 \phi_{PS}(r)}{\phi_{PS}(r)} \right\}. \quad (8)$$

The idea has been numerically tested, and the assumption of  $\lim_{r \rightarrow \infty} V_S(r) = 0$  is indeed appropriate in QCD [19]. We thus estimate the quark kinetic mass from asymptotic behavior of the right-hand side of Eq. (8) in long-distance region.

### III. LATTICE SETUP AND HEAVY QUARKONIUM MASS

#### A. 2 + 1 flavor PACS-CS dynamical gauge ensemble

The computation of the interquark potential for the charmonium ( $c\bar{c}$ ) and charmed-strange ( $c\bar{s}$ ) system is carried out on a lattice  $N_s^3 \times N_t = 32^3 \times 64$  using the 2 + 1 flavor PACS-CS gauge configurations [22]. The gauge fields are generated by non-perturbatively  $\mathcal{O}(a)$ -improved Wilson quark action with  $c_{SW} = 1.715$  [39] and Iwasaki gauge action at  $\beta = 1.90$  [40], which corresponds to a lattice cutoff of  $a^{-1} = 2.176(31)$  GeV ( $a = 0.0907(13)$ fm) [22]. The spatial lattice size is of about  $N_s a \sim 3$  fm. The hopping parameters for the light sea quarks  $\{\kappa_{ud}, \kappa_s\} = \{0.13781, 0.13640\}$  give a pion mass of  $M_\pi = 156(7)$  MeV and a kaon mass of  $M_K = 554(2)$  MeV [22]. Simulation parameters of dynamical QCD simulations used in this work is summarized in Table I. Although the light sea quark masses are slightly off the physical point, the systematic uncertainty due to this fact could be extremely small in this project. Our results are analyzed on all 198 gauge configurations, which are available through International Lattice Data Grid and Japan Lattice Data Grid<sup>3</sup>. Gauge configurations is fixed to the Coulomb gauge.

#### B. Relativistic charm quark

In order to control discretization errors induced by large charm quark mass, we employ the relativistic heavy quark (RHQ) action [23] that removes main errors of  $\mathcal{O}(|\mathbf{p}|a)$ ,  $\mathcal{O}((m_0a)^n)$  and  $\mathcal{O}(|\mathbf{p}|a(m_0a)^n)$  from the on-shell Green’s function. The RHQ action is the anisotropic version of the  $\mathcal{O}(a)$  improved Wilson action with five parameters  $\kappa_c, \nu, r_s, c_B$  and  $c_E$ , called *RHQ parameters* (for more details see Ref. [23, 41]):

$$S_{RHQ} = \sum_x \bar{Q}(x) \left( m_0 a + \gamma_0 D_0 + \nu \boldsymbol{\gamma} \cdot \mathbf{D} - \frac{r_t}{2} a (D^0)^2 - \frac{r_s}{2} a (\mathbf{D})^2 + \sum_{i,j} \frac{i}{4} c_B a \sigma_{ij} F_{ij} + \sum_i \frac{i}{2} c_E a \sigma_{0i} F_{0i} \right) Q(x) \quad (9)$$

where the Wilson parameter for the time derivative is set to be  $r_t = 1$  and the bare quark mass is related to the hopping parameter  $\kappa_c$  as  $am_0 = \frac{1}{2\kappa_c} - r_t - 3r_s$ . The RHQ action utilized here is a variant of the Fermilab approach [42] (See also Ref. [43]).

<sup>3</sup> International Lattice Data Grid/Japan Lattice Data Grid, <http://www.jldg.org>.

TABLE I: Parameters of 2 + 1-flavor dynamical QCD gauge field configurations generated by the PACS-CS collaboration [22]. The columns list number of flavors, lattice volume, the  $\beta$  value, hopping parameters for light and strange quarks, approximate lattice spacing (lattice cut-off), spatial physical volume, pion mass, and number of configurations to be analyzed.

$N_f$	$N_s^3 \times N_t$	$\beta$	$\kappa_{ud}$	$\kappa_s$	$a$ [fm] ( $a^{-1}$ [GeV])	$N_s a$ [fm]	$M_\pi$ [MeV]	# configs.
2 + 1	$32^3 \times 64$	1.9	0.13781	0.13640	0.0907(13) ( $\approx 2.18$ )	2.90(4)	$\approx 156$	198

TABLE II: The hopping parameter  $\kappa_Q$  and RHQ parameters ( $\nu$ ,  $r_s$ ,  $c_B$  and  $c_E$ ) used for the charm quark.

$\kappa_c$	$\nu$	$r_s$	$c_B$	$c_E$
0.10819	1.2153	1.2131	2.0268	1.7911

The parameters  $r_s$ ,  $c_B$  and  $c_E$  in RHQ action are determined by tadpole improved one-loop perturbation theory [41]. For  $\nu$ , we use a nonperturbatively determined value, which is tuned by reproducing the effective speed of light  $c_{\text{eff}}$  to be unity in the dispersion relation  $E^2(\mathbf{p}^2) = M^2 + c_{\text{eff}}^2 \mathbf{p}^2$  for the spin-averaged  $1S$ -charmonium state, since the parameter  $\nu$  is sensitive to the size of hyperfine splitting energy [44]. We choose the value of  $\kappa_c$  to reproduce the experimental spin-averaged mass of  $1S$ -charmonium states  $M_{\text{ave}}^{\text{exp}}(1S) = 3.0678(3)$  GeV. To calibrate RHQ parameters, we employ a gauge invariant Gauss smearing source for the standard two-point correlation function with four finite momenta. As a result, the relevant speed of light in a energy-momentum dispersion relation  $E^2 = M^2 + c_{\text{eff}}^2 \mathbf{p}^2$  is consistent with unity within statistical uncertainties:  $c_{\text{eff}}^2 = 1.04(5)$  for the spin-averaged state [20]. Our chosen RHQ parameters are summarized in Table II.

Using tuned RHQ parameters, we compute the two valence quark propagators with wall sources located at different time slices  $t_s/a = 6$  and  $57$  to increase statistics. Two sets of two- and four-point correlation functions are constructed from the corresponding  $\Gamma$  operator with the charm quark propagator, and folded together to create the single correlation function. Dirichlet boundary conditions are imposed for the time direction at  $t/a = 0$  and  $63$  to eliminate unwanted contributions across time boundaries.

### C. Charmonium spectroscopy from two-point functions

Fig. 1 shows the effective mass of the  $S$ -wave ( $\eta$  and  $J/\psi$ ) and  $P$ -wave ( $\chi_{c0}$ ,  $\chi_{c1}$  and  $h_c$ ) charmonium states calculated from the dynamical lattice QCD simulation. These five charmonium states are classified with quantum numbers  $J^{PC}$  and corresponding operators  $\Gamma$  as shown in Table III. A effective mass is defined as

$$M_\Gamma(t) = \log \frac{G_\Gamma(t, t_s)}{G_\Gamma(t+1, t_s)}. \quad (10)$$

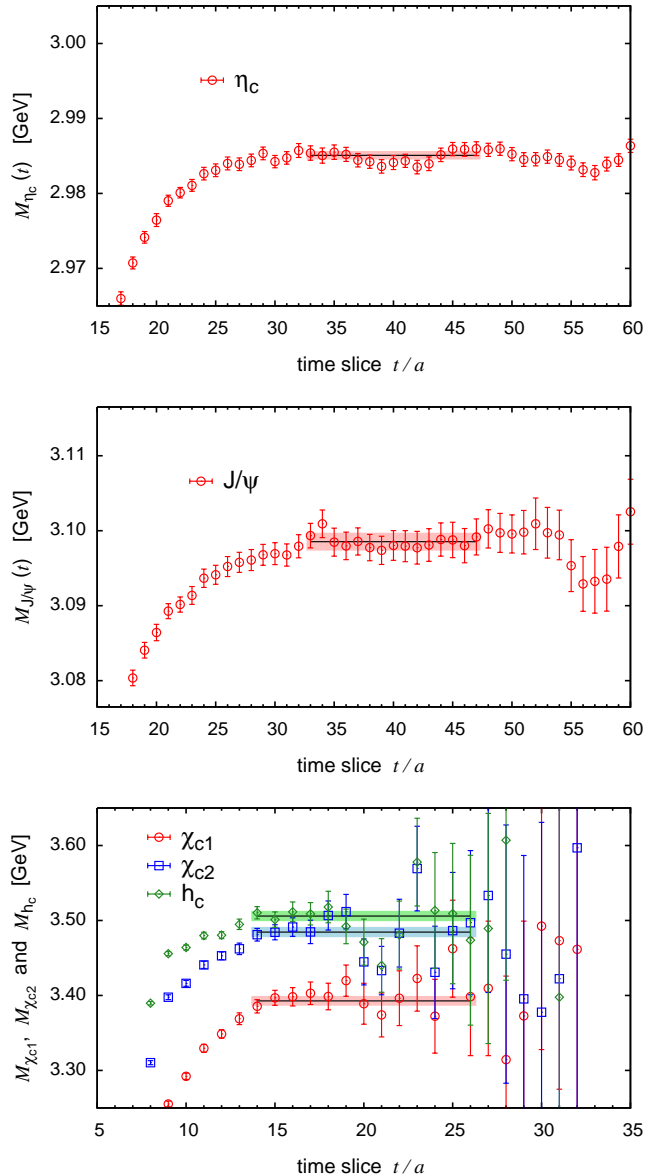


FIG. 1: Effective mass plots for  $\eta_c$  (upper panel),  $J/\psi$  (center panel) and  $1P$  charmonium states ( $\chi_{c0}$ ,  $\chi_{c1}$  and  $h_c$ ) (lower panel). Charmonium states are specified in legend. Solid lines indicate fit results and shaded bands display the fitting ranges and one standard deviations estimated by the jackknife method.

TABLE III: Masses of low-lying charmonium states calculated from two-point functions, the spin-averaged mass and hyperfine splitting energy of  $1S$  charmonium states. Five charmonium states are classified with quantum numbers  $J^{PC}$  and corresponding operators  $\Gamma$ . The fitting ranges and values of  $\chi^2/\text{d.o.f.}$  are also included. Results are given in units of GeV.

state	$(J^{PC})$	$\Gamma$	fit range	mass [GeV]	$\chi^2/\text{d.o.f.}$
$\eta_c$	$(0^{-+})$	$\gamma_5$	[33:47]	2.9851(5)	0.70
$J/\psi$	$(1^{-+})$	$\gamma_i$	[33:47]	3.0985(11)	0.62
$M_{\text{ave}}(1S)$	—	—	—	3.0701(9)	—
$E_{\text{hyp}}(1S)$	—	—	—	0.1138(8)	—
$\chi_{c0}$	$(0^{++})$	1	[14:26]	3.3928(59)	0.66
$\chi_{c1}$	$(1^{++})$	$\gamma_5\gamma_i$	[14:26]	3.4845(62)	1.03
$h_c$	$(1^{+-})$	$\gamma_i\gamma_j$	[14:26]	3.5059(62)	0.63

where  $G_\Gamma(t, t_s)$  is the two-point function obtained by setting  $\mathbf{r}$  to be zero in the four-point function  $G_\Gamma(\mathbf{r}, t, t_s)$  defined in Eq. (3). Each effective mass plot shows a reasonable plateau in the range  $33 \leq t/a \leq 47$  for  $S$ -wave charmonium states and  $14 \leq t/a \leq 26$  for  $P$ -wave charmonium states. We estimate masses of the five charmonium states by a constant fit to the plateau over time ranges shown in Table III. A correlation among effective masses measured at various time slices is taken into account by using a covariance matrix in the fit. An inversion of the covariance matrix is performed once for average and it is used for each jackknife block. The statistical uncertainties indicated by shaded bands in Fig. 1 are estimated by the jackknife method. In Table II, we summarize resultant charmonium masses together with fit ranges used in the fits and values of  $\chi^2$  per degrees of freedom (d.o.f.). Note that all masses calculated in this study are obtained from the Coulomb-gauge wall source propagator, while gauge-invariant Gaussian smeared source was used for results of charmonium masses compiled in Table I of Ref. [19].

Low-lying charmonium masses calculated below  $D\bar{D}$  threshold are all close to the experimental values, though the hyperfine mass splitting  $M_{\text{hyp}} = 0.1124(9)$  GeV is slightly smaller than the experimental value,  $M_{\text{hyp}}^{\text{exp}} = 0.1166(12)$  GeV [45]. The similar value of the hyperfine mass splitting is reported even on the exact physical point in Ref. [44, 46]. Note that here we simply neglect the disconnected diagrams in all two-point correlation functions. The several numerical studies reported that the contributions of charm annihilation to the hyperfine splitting of the  $1S$ -charmonium state is sufficiently small, which is of order 1-4 MeV. [47–49]. At the charm sector, the effect of the disconnected diagrams on the charmonium, especially on the vector state, is perturbatively expected to be small due to Okubo-Zweig-Iizuka suppression.

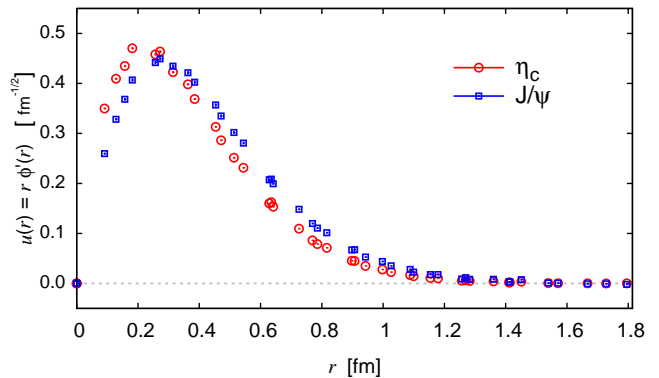


FIG. 2: The reduced  $Q\bar{Q}$  BS wave functions of the  $\eta_c$  (circles) and  $J/\psi$  (squares) states, shown as a function of the spatial distance  $r$ . The data points are taken along  $\mathbf{r}$  vectors which are multiples of three directions  $(1, 0, 0)$ ,  $(1, 1, 0)$  and  $(1, 1, 1)$ .

## IV. DETERMINATION OF INTERQUARK POTENTIAL

### A. $Q\bar{Q}$ BS wave function

We calculate the BS wave functions only for  $S$ -wave states ( $\eta_c$  and  $J/\psi$ ). This is simply because the Coulomb-gauge wall source<sup>4</sup> adopted in this study is not suitable for studying the wave function of  $P$ -wave states, whose spatial part is odd under spatial reflection.

Fig. 2 shows the  $Q\bar{Q}$  BS wave functions of  $1S$ -charmonium states ( $\eta_c$  and  $J/\psi$  states). The BS wave functions are defined by Eq. (2) with a normalization condition of  $\sum \phi_\Gamma^2 = 1$ . We use the reduced wave function  $u_\Gamma(r)$  for displaying the wave function:  $u_\Gamma(r) = r\phi_\Gamma(\mathbf{r})$ . We practically take a time-average of the BS wave function at fixed  $r$  over the range  $33 \leq t/a \leq 47$ , where effective mass plots for  $1S$ -charmonium states show excellent plateaus and excited state contaminations should be negligible. To resolve the strong correlations between data of the BS wave function at different time slices, we take into account the covariance matrix during the averaging process over the time slice.

We find that a breaking of rotational symmetry for the  $Q\bar{Q}$  BS wave functions is sufficiently small in our calculation. The resulting wave functions become isotropic with the help of a projection to the  $A_1^+$  sector of the cubic group that corresponds to the  $S$ -wave in the continuum theory (Fig. 2). All data points of the  $Q\bar{Q}$  BS wave functions calculated in the three different directions fall onto a single curve.

<sup>4</sup> Clearly, the spatial part of the meson operator constructed from a local quark bilinear operator with the wall source, where the quark operator is summed over all spatial sites at given time slice, belongs to the trivial  $A_1^+$  irreducible representation of the cubic group. The plus sign in superscript indicates even parity.

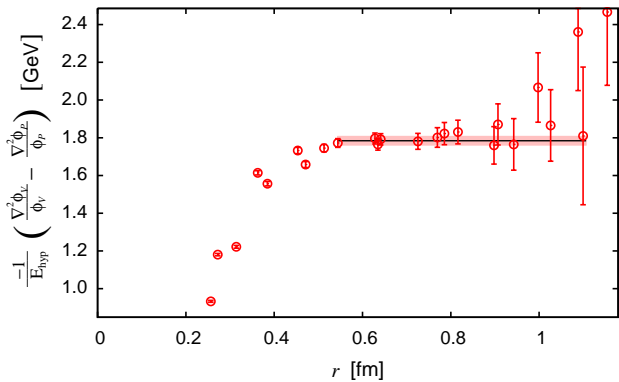


FIG. 3: The determination of quark kinetic mass within the BS amplitude method. The values of  $-(\nabla^2\phi_V/\phi_V - \nabla^2\phi_{PS}/\phi_{PS})/E_{\text{hyp}}$  as a function of the spatial distance  $r$  are shown in this figure. The quark kinetic mass  $m_Q$  is obtained from the long-distance asymptotic values of  $-(\nabla^2\phi_V/\phi_V - \nabla^2\phi_{PS}/\phi_{PS})/E_{\text{hyp}}$ . Horizontal solid line indicates a value of quark kinetic mass obtained by fitting a asymptotic constant in the range  $0.54 \text{ fm} \lesssim r \lesssim 1.10 \text{ fm}$ . A shaded band indicates a statistical error estimated by the jackknife method.

The spatial lattice extent  $N_s a \approx 2.9 \text{ fm}$  is sufficiently large enough to study the  $1S$ -charmonium system. Indeed, the BS wave functions shown in Fig. 2 are localized around the origin and vanished at  $r \gtrsim 1.1 \text{ fm}$ . It suggests that the  $Q\bar{Q}$  BS wave functions for the  $\eta_c$  and  $J/\psi$  states fair enough fit into the box  $N_s^3$ . Needless to say, the localized wave functions is interpreted as a sign of bound states. This fact however reminds us that the interquark potential can be deduced within the interior of the hadron due to its localized wave function. This is simply because that the signal-to-noise ratio in the calculation of  $\nabla^2\phi/\phi$  of Eq. (6)-(8) is getting worse outside the spatial size of the hadron.

Other important information can be read off from Fig. 2. The spatial size of the  $J/\psi$  state is slightly larger than that of the  $\eta_c$  state. This indicates that there is a repulsive spin-spin interaction near the origin for the higher spin states. It is consistent with the pattern of level ordering for the hyperfine multiplet. The spin-spin charmonium potential will be discussed in more detail later.

## B. quark kinetic mass

In our formalism, the kinetic mass of the charm quark is determined self-consistently within the BS amplitude method as well [19]. According to Eq. (8), the quark kinetic mass can be evaluated from an asymptotic behavior of the quantity  $-(\nabla^2\phi_V/\phi_V - \nabla^2\phi_{PS}/\phi_{PS})/E_{\text{hyp}}$  at long distances. For the discrete Laplacian operator  $\nabla^2$ , we use  $r$ -Laplacian, which is defined in polar coordinates

as follows:

$$\nabla^2\phi_\Gamma(r) = \frac{2}{r} \frac{\phi_\Gamma(r+\tilde{a}) - \phi_\Gamma(r-\tilde{a})}{2\tilde{a}} + \frac{\phi_\Gamma(r+\tilde{a}) + \phi_\Gamma(r-\tilde{a}) - 2\phi_\Gamma}{\tilde{a}^2} \quad (11)$$

where  $r$  is the absolute value of the relative distance as  $r = |\mathbf{r}|$ , and  $\tilde{a}$  is a spacing between grid points along differentiate directions. In the on-axis direction  $\mathbf{r} \propto (1,0,0)$  (labeled by “on-axis”), two off-axis directions  $\mathbf{r} \propto (1,1,0)$  (labeled by “off-axis I”) and  $\mathbf{r} \propto (1,1,1)$  (labeled by “off-axis II”), the effective grid spacings correspond to  $\tilde{a} = a, \sqrt{2}a$  and  $\sqrt{3}a$ , respectively. The difference of ratios  $\nabla^2\phi_\Gamma/\phi_\Gamma$  at each  $r$  are obtained by a constant fits to the lattice data with reasonable  $\chi^2/\text{d.o.f.}$  values over the range of time slices where two-point functions exhibit the plateau behavior ( $33 \leq t/a \leq 47$ ).

Fig. 3 illustrates the determination of quark kinetic mass  $m_Q$  for the charmonium system. The value of  $m_Q$  can be determined from an asymptotic value of  $-(\nabla^2\phi_V/\phi_V - \nabla^2\phi_{PS}/\phi_{PS})/E_{\text{hyp}}$  in the range of  $6 \leq r/a \leq 7\sqrt{3}$  ( $0.54 \text{ fm} \lesssim r \lesssim 1.10 \text{ fm}$ ), where  $V_S(r)$  should vanish. In this study, three data sets are obtained from three directions: on-axis, off-axis I and off-axis II, are separately analyzed so as to expose the size of the possible lattice discretization artifacts. On each data set, a value of  $m_Q$  is obtained by a constant fit to a long-distance asymptotic value over the range as described above. Finally we average them over three directions, and then obtain  $m_Q = 1.784(23)(6)(20) \text{ GeV}$ . The first error is statistical, given by the jackknife analysis. In the second error, we quote a systematic uncertainty due to rotational symmetry breaking by taking the largest difference between average value and individual ones obtained for specific directions. The third ones are systematic uncertainties stemming from choice of  $t_{\text{min}}$  in the averaging process over the time-slice range  $t_{\text{min}}/a \leq t/a \leq 47$ . The minimum time-slice  $t_{\text{min}}/a$  is varied over range from 33 to 41 and then take a largest difference from the preferred determination of  $m_Q$ .

The charm quark mass obtained in this study is somewhat heavier than the usual quark kinetic mass in the NRp models. For example, the quark kinetic mass adopted in Ref. [4] is about 17% smaller. This difference however should not be taken seriously, because the value of  $m_Q$  in the NRp models highly depends on a constant term  $V_0$  of the Cornell potential, and  $V_0$  is actually forced to be zero in many of the NRp models. In addition, the spatial profile of the spin-spin potential from lattice QCD is slightly different from the one used in the NRp models as we will discuss later.

## C. Spin-independent interquark potential

Once the quark kinetic mass is determined, we can calculate the central spin-independent and spin-spin charmonium potentials from the  $Q\bar{Q}$  BS wave function

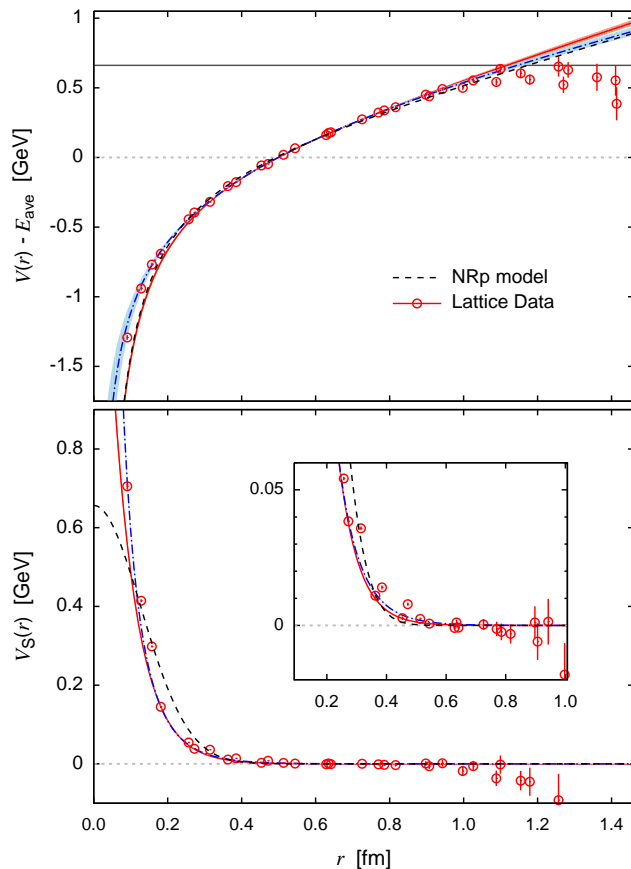


FIG. 4: Central spin-independent and spin-spin charmonium potentials calculated from the BS wave functions in the dynamical QCD simulation with almost physical quark masses. In the upper panel, we show the spin-independent potential  $V(r)$ . A solid (dot-dashed) curve is the fit results with the Cornell (Cornell plus log) form. The shaded bands show statistical uncertainties in the fitting procedure where the jack-knife method is used. Note that the spin-averaged mass of  $1S$ -charmonium states  $E_{\text{ave}}$  is not subtracted in this figure. A horizontal line indicates the level of open-charm ( $D^0\bar{D}^0$ ) threshold  $\approx 3729$  MeV. In the lower panel, we show the spin-spin potential  $V_S(r)$ . A solid (dot-dashed) curve corresponds to fitting results with exponential (Yukawa) form. The inset shows a magnified view. In both panels, the phenomenological potentials adopted in a NRp model [4] are also included as dashed curves for comparison.

TABLE IV: Summary of the Cornell parameters and the quark mass determined by the BS amplitude method. For comparison, ones adopted in a phenomenological NRp model [4] and ones of the static potential obtained from Polyakov line correlations are also included. In the first column, the quoted errors indicate the sum of the statistical and systematic added in quadrature.

	This work	Polyakov lines	NRp model [4]
$A$	0.713(83)	0.476(81)	0.7281
$\sqrt{\sigma}$ [GeV]	0.402(15)	0.448(16)	0.3775
$m_Q$ [GeV]	1.784(31)	$\infty$	1.4794

through Eq. (6) and Eq. (7). First, we show a result of the spin-independent charmonium potential  $V(r)$  in the upper panel of Fig. 4. The constant energy shift  $E_{\text{ave}}$  is not subtracted in this figure. As we reported in Ref [20], the charmonium potential calculated by the BS amplitude method from dynamical lattice QCD simulations properly exhibits the linearly rising potential at large distances and the Coulomb-like potential at short distances. At first glance, the data points of the charmonium potential obtained from lattice QCD roughly follow the phenomenological potential used in the NRp models, which is represented by the dashed curve. Nevertheless, the data points at short distances are slightly off the dashed curve. In addition, a *string breaking-like behavior* is found in the range  $r \lesssim 1.1$  fm, where the charmonium potential reaches the level of open-charm threshold. We will discuss this point later, and for a while we concentrate only on data points in the range  $r \lesssim 1.1$  fm, where the linearly rising potential is clearly visible.

For more close comparison, as a first step, we simply adopt the Cornell parametrization to fit the data of the spin-independent central potential:

$$V(r) = -\frac{A}{r} + \sigma r + V_0 \quad (12)$$

with the Coulombic coefficient  $A$ , the string tension  $\sigma$ , and a constant  $V_0$ . All fits are performed individually for each three directions over the range  $[r_{\text{min}}/a : r_{\text{max}}/a] = [4 : 7\sqrt{3}]$ , where  $r_{\text{max}} \approx 1.1$  fm. We minimize the  $\chi^2/\text{d.o.f.}$  with the covariance matrix and get the Cornell parameters of the charmonium potential as  $A = 0.713(26)(38)(31)(62)$  and  $\sqrt{\sigma} = 0.402(6)(4)(9)(9)$  MeV with  $\chi^2/\text{d.o.f.} \approx 3.2$ . The first error is statistical, and the second, third and fourth ones are systematic uncertainties due to the choice of data points taken from three directions, and variations of  $t_{\text{min}}$  and  $r_{\text{min}}$ , respectively.

The resulting Cornell parameters are summarized in Table IV. We also include both phenomenological ones adopted in a NRp model [4] and ones of the static potential obtained from Polyakov-line correlators. The latter is estimated using the same method as in Ref. [22]. Additionally, we calculate the Sommer parameter defined as  $r_0 = \sqrt{(1.65 - A)/\sigma}$ , and then obtain the value of  $r_0 = 0.476(6)(11)(3)(6)$  fm, which is fairly consistent with the value quoted in Ref. [22].

From our previous research in quenched QCD [21], the finite  $m_Q$  corrections could be encoded into the Cornell parameters. Indeed, as shown in Table IV, in the charmonium potential from the BS wave function, a Coulomb-like behavior is enhanced and the linearly rising force is slightly reduced due to finite charm quark mass effects in comparison to the conventional static potential from Wilson loops or Polyakov-line correlators. Furthermore, a gap for the Cornell parameters between the static and the phenomenological potentials seems to close by our new approach, which nonperturbatively accounts for a finite quark mass effect.



Here, we give a few technical remarks on the systematic uncertainties on the Coulombic coefficient  $A$ , which highly depends on the choice of minimum value  $r_{\min}$  of the fitting window compared to the string tension  $\sigma$ . This is simply because the linear part in the Cornell potential parametrization is dominated in the region in which we have data points. Indeed, as shown in the upper panel of Fig. 4, a solid curve, which corresponds to fitting results with the Cornell potential form, does not describe well data points outside the range  $[r_{\min} : r_{\max}]$  used in the fit.

In order to provide an adequate fit to the data points at shorter distances, we employed several alternative fitting forms. We found that a simple extension of the Cornell potential can describe the behavior of our charmonium potential reasonably well. An alternative fitting form is given such that a log term is added to the Cornell potential:

$$V(r) = -\frac{A}{r} + \sigma r + V_0 + B \log(r\Lambda) \quad (13)$$

where the value of  $\Lambda$  is simply set to be lattice cutoff  $a^{-1}$ . Such a logarithmic  $r$ -dependence may appear in the leading  $1/m_Q$  correction to the static potential as reported in Ref. [50]. Moreover, as reported in Ref. [51], the charmonium potential obtained from the BS amplitude is consistent with the  $Q\bar{Q}$  potential obtained in the Wilson-loop approach within errors, when a leading  $1/m_Q$  correction calculated in Ref. [52] is added to the static potential from Wilson loops.

A fit with the ‘‘Cornell-plus-log’’ form (13) leads to the values of  $A = 0.194(137)(33)(36)(66)$ ,  $\sqrt{\sigma} = 0.300(38)(19)(20)(21)$  GeV and  $B = 0.390(113)(20)(39)(61)$  GeV with the slightly smaller value of  $\chi^2/\text{d.o.f.} \approx 2.3$ . We here chose the fitting range to be  $[r_{\min}/a : r_{\max}/a] = [3 : 7\sqrt{3}]$  and used a covariance matrix for taking into account the correlation among data points in the fit. The quoted errors have the same meaning as described above.

We also plot the fit result with the Cornell-plus-log form, which is represented by a dot-dashed curve, in upper panel of Fig. 4. The shaded band displays one standard deviation estimated by the jackknife method. The short-distance behavior of the charmonium potential is better described by the Cornell-plus-log form than the Cornell form (solid curve). If compared with the phenomenological potential of the NR models, the shape of the fitted curve of the Cornell-plus-log form at long-distances are much in agreement with the NR models though the string tension  $\sigma$  becomes a slightly smaller value compared with the phenomenological one. In this context, the inclusion of the log term into the Cornell form gives only a minor modification at long-distances as far as the data is accessible in this study.

Finally, we would like to comment on the *string breaking-like* behavior appeared in the range  $r \gtrsim 1.1$  fm. Although in principle, string breaking due to the presence of dynamical quarks is likely to be observed, the observed feature in this study is suspicious and unreli-

TABLE V: Results of fitted parameters for the spin-spin potential with the exponential and Yukawa forms. The quoted errors are statistical only. In the case of the spin-spin potential, we use only the on-axis data.

Functional form	$\alpha$	$\beta$	$\chi^2/\text{d.o.f.}$
Exponential	2.15(7) GeV	2.93(3) GeV	2.0
Yukawa	0.815(27)	1.97(3) GeV	1.7

able. As mentioned previously, the signal-to-noise ratio on the quantity of  $\nabla^2 \phi_\Gamma / \phi_\Gamma$  becomes worse rapidly as the spatial distance  $r$  increases because of the localized nature of the BS wave function  $\phi_\Gamma(r)$ . Moreover, the lattice data of the potential near the spatial boundaries are also sensitive to the possible distortion of its spatial profile as finite volume effects. Therefore, at least, calculations of the higher charmonium near the open charm threshold using a larger lattice is necessary for observing the string breaking in this sense. Their wave functions are extended until the string breaking sets in.

We also emphasize that there might be another possible reason for no evidence of string breaking from a view point of studies within the Wilson loop approach [53–56]. The string breaking in the static heavy quark potential can be observed only after inserting a operator of light quark-antiquark to create the heavy-light meson-antimeson state  $(Q\bar{q})(q\bar{Q})$ , because the  $Q\bar{Q}$  creation operator poorly overlaps with  $|(Q\bar{q})(q\bar{Q})\rangle$  state in Fock space [57–59] (See also Ref. [60] in the case of nonzero temperature). It is worth reminding that the static potential from Wilson loops is regarded as the ‘‘energy eigenvalue’’ of the considering states. There would be nothing to change for the charmonium potential extracted from the ‘‘stationary’’ wave function of the charmonium state, which is well defined in the BS amplitude method unless its energy level is above the open-charm threshold.

#### D. Spin-Spin potential

The lower panel in Fig. 4 shows the spin-spin charmonium potential obtained from the BS amplitude method with almost physical quark masses. The spin-spin potential exhibits the short-range *repulsive interaction*, which is required to lead to energy gain for the higher spin state. Recall that the Wilson loop approach currently does not achieve to reproduce the correct behavior of the spin-spin interaction. The leading-order spin-spin potential classified in pNRQCD becomes attractive at short distances [17, 18]. Their calculation at next-to-leading order is unavailable at present. In contrast of the case of the spin-independent potential, the spin-spin potential obtained from the BS wave function is absolutely different from a repulsive  $\delta$ -function potential generated by perturbative one-gluon exchange [5]. Such contact form  $\propto \delta(\mathbf{r})$  of the Fermi-Breit type potential is widely

adopted in the NRp models [3, 61].

The pointlike spin-spin interaction easily lifts the mass degeneracy between  $1^1P_1$  state ( $h_c$ ) and spin-weighted average of  $1^3P_J$  states ( $\chi_{cJ}$ );  $M(\overline{1^3P_J}) = (M_{\chi_{c0}} + 3M_{\chi_{c1}} + 5M_{\chi_{c2}})/9$ . On the other hand, a finite-range interaction gives a non-zero, but small finite hyperfine splitting to the  $P$ - or higher-wave charmonia [7]. In the current experiments, however, the splitting  $M_{\text{hyp}}(1P) = M(\overline{1^3P_J}) - M_{h_c}$  for  $1P$ -charmonium states is not appreciably observed within experimental error. Here we quote  $M_{\text{hyp}}(1P) = 0.02 \pm 0.19(\text{stat}) \pm 0.13(\text{syst})$  MeV from the CLEO experiment [62, 63] (See also Ref. [64]).

The  $Q\bar{Q}$  interaction is not entirely due to one-gluon exchange so that the spin-spin potential is not necessary to be a simple contact form  $\propto \delta(\mathbf{r})$  [65–68]. This is shown to be true even for the  $\mathcal{O}(1/m_Q^2)$  spin-spin corrections in the Wilson-loop approach [17, 18], regardless of the sign issue. In the phenomenological side, the finite-range spin-spin potential described by the Gaussian form is adopted by some NRp model in Ref. [4], where many properties of conventional charmonium states at higher masses are predicted. This phenomenological spin-spin potential is also plotted in the lower plot of Fig. 4 for comparison. There is a slight difference at very short distances, although the range of spin-spin potential calculated from the BS amplitude method is similar to the phenomenological one.

To examine an appropriate functional form for the spin-spin potential, we try to fit the data with several functional forms, and explore which functional form can give a reasonable fit over the range of  $r/a$  from 2 to  $7\sqrt{3}$ . As a results, the long-range screening observed in the spin-spin potential is accommodated by the exponential form and the Yukawa form:

$$V_S(r) = \begin{cases} \alpha \exp(-\beta r) & : \text{Exponential form} \\ \alpha \exp(-\beta r)/r & : \text{Yukawa form} \end{cases} \quad (14)$$

All results of correlated  $\chi^2$  fits are summarized in Table V. We also try to fit with the Gaussian form that is often employed in the NRp models, and it however gives an unreasonable  $\chi^2/\text{d.o.f.}$  value. Note that we here use only the on-axis data which are expected to less suffer from the rotational symmetry breaking and the discretization error, because fit results to the lattice data taken in each direction significantly disagree with each other [21]. We need the finer lattice to have a solid conclusion to the shape of the spin-spin potential and the uncertainties due to the rotational symmetry breaking.

## V. CHARMONIUM MASS SPECTRUM FROM CHARMONIUM POTENTIAL

Once the quark kinetic mass and the charmonium potentials are determined by first principles of QCD, we can solve the nonrelativistic Schrödinger equation defined with the theoretical inputs for the bound  $c\bar{c}$  systems as same as calculations in the NRp models [2, 65, 66, 69].

In the non-relativistic description, each charmonium state is generally labeled by a symbol  $^{2S+1}[L]_J$ , with the spin angular momentum ( $S = 0, 1, \dots$ ), the orbital angular momentum ( $[L] = S, P, D, \dots$  corresponding to  $L = 0, 1, 2, \dots$ ) and the total angular momentum ( $J = S \oplus L$ ) quantum numbers. The  $J^{PC}$  notation is also used to classify the charmonium state. The parity ( $P$ ) and the charge-conjugation ( $C$ ) are given by  $P = (-1)^{L+1}$  and  $C = (-1)^{S+L}$  within the non-relativistic description.

Recall that all of the charmonium states below the open-charm threshold are experimentally well established [45]. The last missing  $1P$ -charmonium state,  $h_c$ , and also the first excited state of the pseudoscalar  $1S$ -charmonium state,  $\eta_c(2S)$ , have already been observed in recent experiments [62, 63, 70–75].

In this section, we will discuss whether we can get the correct low-lying charmonium spectra within *the hybrid approach* between lattice QCD simulations and the NRp models in comparison to experimental data. In addition, we also perform a consistency check between two different methods in lattice QCD to verify the validity of our approach. One is of course the standard lattice spectroscopy, where the mass information is extracted from the large-time asymptotic behavior of the two-point correlation functions, while another mainly uses the information about the spatial profile of the BS amplitudes. In this sense, these two methods are essentially different.

### A. Nonrelativistic Hamiltonian from lattice QCD

For solving a nonrelativistic Schrödinger equation, the constant energy shift is irrelevant. We here introduce the energy-shifted potential in the spin-independent part as  $V'(r) = V(r) - E_{\text{ave}}$  for the following reason: The quantity of  $V'(r)$  can be directly obtained from the BS amplitudes of  $1S$ -charmonium states except the overall factor of  $1/m_Q$ . It ends up with less statistical uncertainties compared to the original potential  $V(r)$ , whose estimation requires the subtraction of  $E_{\text{ave}}$ . This is simply because the value of  $E_{\text{ave}} = M_{\text{ave}} - 2m_Q$  receives somewhat large uncertainties, which arise mainly in the determination of  $m_Q$  through Eq. (8). Indeed, when we evaluate a difference between  $V_0$  and  $E_{\text{ave}}$  directly from the fit with the Cornell functional form to the data of  $V'(r)$ , this quantity shows much smaller error such as  $V_0 - E_{\text{ave}} = -0.146(13)$  GeV, in comparison to the values of  $E_{\text{ave}} = 0.508(69)$  GeV and  $m_Q = 1.789(34)$  GeV.

We therefore adopt the energy-shifted potential of  $V'(r)$  to reduce uncertainties on the final result for energy eigenvalues, and then solve the following Schrödinger

equation for the reduced wave function  $u_{SLJ}(r)$ <sup>5</sup>:

$$\left\{ -\frac{\nabla^2}{m_Q} + \frac{L(L+1)}{m_Q r^2} + V'_{SLJ}(r) \right\} u_{SLJ}(r) = E'_{SLJ} u_{SLJ}(r) \quad (15)$$

where  $V'_{SLJ}(r) = V_{SLJ}(r) - E_{\text{ave}}$  and  $E'_{SLJ} = E_{SLJ} - E_{\text{ave}}$  with angular momentum quantum numbers ( $S$ ,  $L$  and  $J$ ). The interquark potentials  $V'_{SLJ}(r)$ , which may involve the spin-dependent interactions, clearly depend on the charmonium states labeled with specific  $S$ ,  $L$  and  $J$ . The rest mass energy of the desired charmonium state is obtained simply by adding the energy eigenvalue of  $E'_{SLJ}$  to the spin-averaged  $1S$ -charmonium mass of  $M_{\text{ave}}$ , which is evaluated by the standard lattice spectroscopy with high accuracy:  $M_{SLJ} = M_{\text{ave}} + E'_{SLJ} = 2m_Q + E_{SLJ}$ .

The potential calculated from lattice QCD with the BS amplitude method are by definition discretized in space. In this context, instead of the continuum Schrödinger equation, we practically solve eigenvalue problems of finite-dimensional vector  $u_n = u(n\tilde{a})$  and finite-dimensional matrix [76] as

$$\sum_{n>0} H_{m,n} u_n = E' u_m. \quad (16)$$

Note that a summation of  $n$  does not include  $n = 0$  since the reduced wave function is required to vanish at the origin. In the symmetric matrix  $H_{m,n}$  for  $n, m > 0$ , diagonal and off-diagonal matrix elements are given by

$$H_{n,n} = \frac{1}{\tilde{a}^2 m_Q} \left[ 2 + \frac{L(L+1)}{n^2} \right] + V'(n\tilde{a}), \quad (17)$$

$$H_{n\pm 1,n} = -\frac{1}{\tilde{a}^2 m_Q}, \quad (18)$$

and all other elements are zero. Here we omit the labels  $SLJ$  for clarity.

In this work, we separately solve Eq. (16) in the directions of vectors  $\mathbf{r}$  which are multiples of  $(1, 0, 0)$ ,  $(1, 1, 0)$  and  $(1, 1, 1)$ . We prefer to use mainly on-axis data, which is expected to receive smallest discretization error and correction due to rotational symmetry breaking as studied in Ref. [21], and take the largest difference between on-axis and off-axis results as the systematic error due to the choice of the  $\mathbf{r}$  direction, while statistical errors are estimated by the jackknife method. Systematic uncertainties stemming from the choice of the fitting window in the averaging process over the time-slice range are smaller than other errors.

Alternatively, we may solve the continuum Schrödinger equation with the parameterized charmonium potential

<sup>5</sup> Here, we assume that the reduced wave function vanishes at origin  $\lim_{r \rightarrow 0} r \phi'(r) = u(r) = 0$ . Indeed, if the potential satisfies  $r^2 V(r) \xrightarrow{r \rightarrow 0} 0$ , one can easily show the reduced wave function asymptotically behaves as  $u(r) \xrightarrow{r \rightarrow 0} r^{L+1}$ .

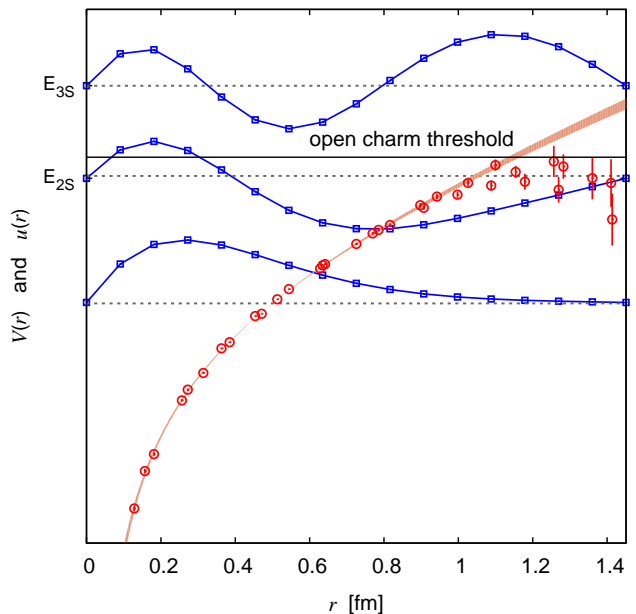


FIG. 5: The energy-levels (dotted lines) and corresponding reduced wave functions  $u(r)$  (squares) of spin-averaged  $1S$ -charmonium states, obtained by solving the Schrödinger equation with the lattice inputs. Only the central (average) values are shown for both quantities. A horizontal line indicates the open-charm threshold. The spin-independent charmonium potential obtained from lattice QCD and its fitting result with the Cornell-plus-log functional form as a function of  $r$  are also overlaid in the same plot as circles and a shaded band, respectively.

by empirical functional forms such as the Cornell form or the Cornell-plus-log form as discussed in Sec. IV. This procedure, however, yields large uncertainties in the low-lying energy levels, which highly depend on the choice of functional forms especially at short distances. To avoid such model dependence, we adopt the former strategy, which does not suffer from the sensitivity to the shape of the potential at short distances.

## B. Wave functions solving the Schrödinger equation

In Fig 5, we plot energy-levels (dotted lines) and corresponding reduced wave functions (curves with square symbols) up to the second excited state for the spin-averaged  $S$ -wave charmonium states, which are given by the charmonium potential with an expectation value of the spin operator being zero,  $\langle \mathbf{S}_Q \cdot \mathbf{S}_{\bar{Q}} \rangle = 0$ . The spin-independent charmonium potential, which is calculated from lattice QCD, is also overlaid in the figure as circle symbols together with its fitting result using the Cornell-plus-log form (shaded band).

We first carefully examine the energy eigenvalue  $E'_{\text{ave}}$  of the spin-averaged  $1S$  charmonium state whose mass

was used as input to calibrate the RHQ parameters for the charm quark. Recall that the value of  $E'_{\text{ave}}$  is supposed to be zero because of its definition on the shifted energy  $E'$  introduced in Eq. (15). We consequently obtain  $E'_{\text{ave}} = 0.2(1.3)(0.5)$  MeV, where the first error is statistical, the second error is systematic error due to rotational symmetry breaking. The obtained value is sufficient for satisfying the condition  $E'_{\text{ave}} = 0$  as a self-consistency check in our approach. We then conclude that the spin-averaged  $1S$ -charmonium state can be well described by our charmonium potential given in the range  $r \lesssim 1.1$  fm.

The boundary condition implemented in the definition of the Hamiltonian matrix defined in Eq. (16) enforces the wave functions to vanish outside the interval  $r \leq \tilde{a}N_s/2$ . Although our choice of  $N_s/2 \times N_s/2$  for the size of Hamiltonian matrix  $H_{n,m}$  is large enough for the  $1S$ -charmonium states as discussed above, the higher-lying states that have more extended wave functions seem to suffer from the finite size effect caused by the boundary condition. Indeed, the resulting wave functions of the  $2S$  and  $3S$  charmonium states might be somewhat squeezed due to the smaller size of  $\tilde{a}N_s/2$ . Therefore, these energy levels would be pushed down slightly due to the shrinkage of wave functions being less affected by the confining potential. As we mentioned above, the lattice data of the spin-independent potential becomes noisy in the range  $r \gtrsim 1.1$  fm, where signal-to-noise ratio of the BS wave function is poor, and also suffers from the finite volume effect in lattice QCD simulations. In order to draw a firm conclusion for properties of higher-lying charmonium states without these effects, we clearly need to extend the calculation of the charmonium potential derived from the ground state wave function to the higher-lying states such as  $2S$  and  $3S$  states, which have more extended wave functions, using a sufficiently large lattice.

### C. Chromium mass spectrum

We show the charmonium spectrum below 4200 MeV in Fig. 6. Theoretical spectra plotted as rectangular shaded boxes are given by solving the discrete nonrelativistic Schrödinger equations with the theoretical inputs. Vertical box length represents the level of uncertainty, which is given by adding statistical and systematic errors in quadrature. For the purpose of comparison, we plot both experimental values (horizontal lines) and results of the standard lattice spectroscopy (square symbols) together. The experimental values are taken from Particle Data Group [45]. At first glance, one can find that below the open charm threshold, our theoretical calculations from the NRp model with the lattice inputs excellently agree with not only the lattice spectroscopy, but also experiments. Especially a agreement between two lattice results provides a strong check for the validity of our new method. All results including the lattice spectroscopy results are also summarized together with the experimental

TABLE VI: Masses of the charmonium states below 4200 MeV are summarized in units of MeV. The labels of AVE and HYP in a column of “state” for  $S$ -wave states denotes the spin-averaged mass  $(M_{1S_0} + 3M_{3S_1})/4$  and hyperfine splitting mass  $M_{3S_1} - M_{1S_0}$ . Experimental data (denoted as Exp.) in the second column are taken from Particle Data Group, rounded to 1 MeV [45]. There are two kinds of lattice QCD results tabulated in the third and fourth columns. One is obtained by the standard lattice spectroscopy, while another is evaluated by solving the Schrödinger equation with the charmonium potential determined from lattice QCD. For the latter, the first error is statistical and the second error systematic as described in text. The spin-weighted average mass (denoted as  ${}^3[L]_J$ ) are also included for spin triplet states  ${}^3[L]_J$ . The last column shows the results from a NRp model [4].

state	Exp.	Lattice QCD		NRp model [4]
		spectroscopy	BS amplitude	
$\eta_c$ ( $1^1S_0$ )	2981	2985(1)	2985(2)(1)	2982
$J/\psi$ ( $1^3S_1$ )	3097	3099(1)	3099(2)(1)	3090
AVE	3068	3070(9)	3070(2)(1)	3063
HYP	116	114(1)	113(1)(0)	108
$\eta_c$ ( $2^1S_0$ )	3639		3612(9)(7)	3630
$\psi$ ( $2^3S_1$ )	3686		3653(12)(5)	3672
AVE	3674		3643(11)(5)	3662
HYP	47		41(6)(3)	42
$\eta_c$ ( $3^1S_0$ )			4074(20)(70)	4043
$\psi$ ( $3^3S_1$ )	4039		4099(24)(98)	4072
AVE			4092(22)(91)	4065
HYP			25(15)(28)	29
$h_c$ ( $1^1P_1$ )	3525	3506(6)	3496(7)(19)	3516
$\overline{\chi_{cJ}}$ ( $1^3P_J$ )	3525		3503(7)(10)	3524
$\chi_{c0}$ ( $1^3P_0$ )	3415	3393(6)		3424
$\chi_{c1}$ ( $1^3P_1$ )	3511	3485(6)		3505
$\chi_{c2}$ ( $1^3P_2$ )	3556			3556
$h_c$ ( $2^1P_1$ )			3927(16)(34)	3934
$\overline{\chi_{cJ}}$ ( $2^3P_J$ )			3916(19)(31)	3943
$\chi_{c0}$ ( $2^3P_0$ )	3918			3852
$\chi_{c1}$ ( $2^3P_1$ )				3925
$\chi_{c2}$ ( $2^3P_2$ )	3927			3972
$\eta_{c2}$ ( $1^1D_2$ )			3783(12)(4)	3799
$\overline{\psi}$ ( $1^3D_J$ )			3774(13)(2)	3800
$\psi$ ( $1^3D_1$ )	3773			3785
$\psi$ ( $1^3D_2$ )				3800
$\psi$ ( $1^3D_3$ )				3806
$\eta_{c2}$ ( $2^1D_2$ )			4221(21)(72)	4158
$\overline{\psi}$ ( $2^3D_J$ )			4193(25)(88)	4159
$\psi$ ( $2^3D_1$ )	4153			4142
$\psi$ ( $2^3D_2$ )				4158
$\psi$ ( $2^3D_3$ )				4167

values in Table VI.

In this study, we have succeeded in extracting *only the spin-spin potential* among the spin-dependent parts of the interquark potential. Thus at this stage we cannot predict the spin-orbit splitting which is led by the tensor and spin-orbit terms of the spin-dependent potential. In other words, we can compute only the *spin-averaged mass*

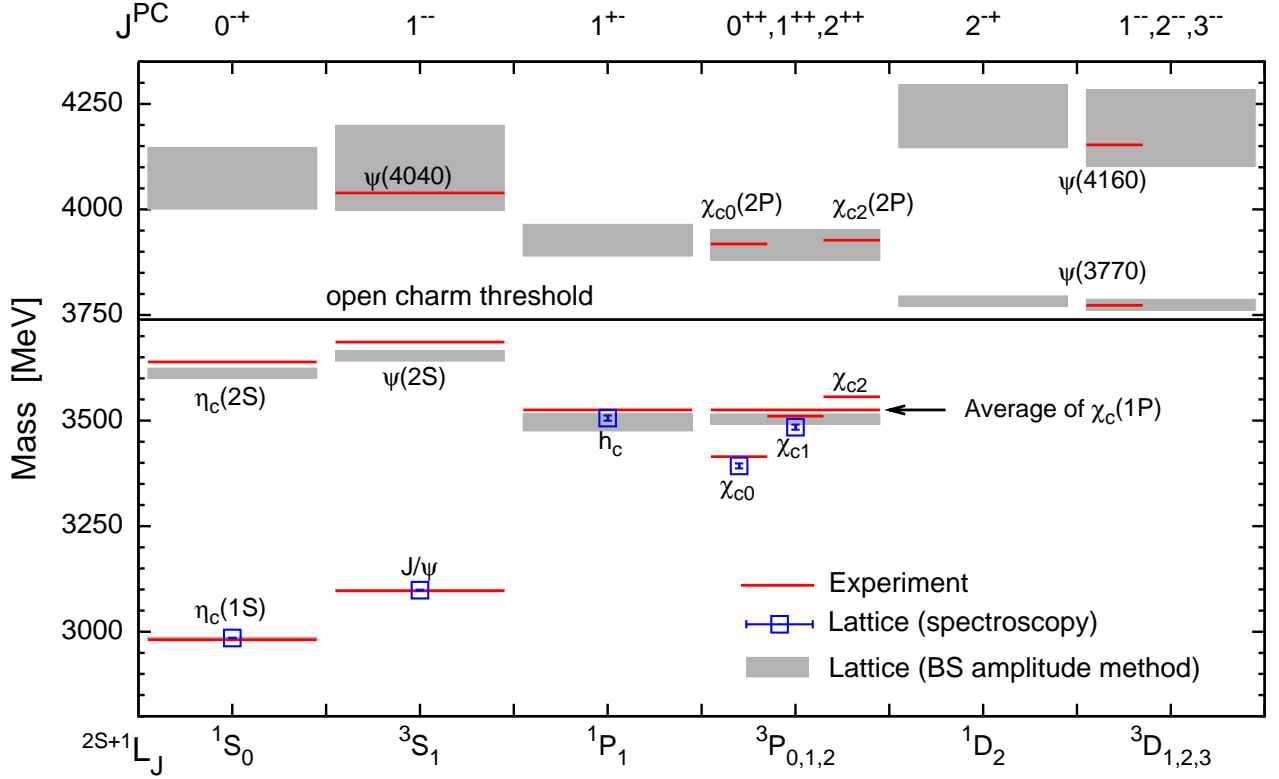


FIG. 6: Mass spectrum of charmonium states below and near the open-charm threshold. The vertical scale is in units of MeV. Labels of  $^{2S+1}[L]_J$  ( $J^{PC}$ ) are displayed in the lower (upper) horizontal axis. Rectangular shaded boxes indicate predictions from the NRp model with purely theoretical inputs based on lattice QCD and their errors which are the sum of the statistical and systematic added in quadrature. Solid lines indicate experimental values of well established charmonium states, while square symbols represent results of the standard lattice spectroscopy. A horizontal solid line shows the open-charm threshold. A symbol of  $\overline{^3P_J}$  denotes the spin-weighted average of spin-triplet  $^3P_J$  states whose mass is given by  $M_{\overline{\chi_{cJ}}} = (M_{\chi_{c1}} + 3M_{\chi_{c2}} + 5M_{\chi_{c3}})/9$ .

for higher-wave charmonium states like  $P$ -wave charmonium  $\chi_{cJ}$  state.

The mass splitting between the radial excitations and the ground state also provides an important validity check on our new approach. Fig. 7 shows several mass splittings theoretically predicted by the hybrid approach in comparison to physical values of the corresponding splittings. In the top left panel of Fig. 7, the radial excitation mass splitting of the spin-averaged  $1S$  and  $2S$  states is  $M_{\text{ave}}(2S) - M_{\text{ave}}(1S) = 573(10)(5)$  MeV, of which value is slightly smaller than the experimental value of  $606(1)$  MeV [45]. This deviation ( $\sim 30$  MeV) from the experiment can be attributed to the finite volume effect, which is caused by the fact that more extended  $2S$  state than  $1S$  state is forced to fit in the spatial volume  $\sim (3 \text{ fm})^3$ . Note that the  $S$ - $D$  mixing due to the tensor force is simply ignored in our calculations. Thus, the spin-spin potential solely gives the mass splitting in hyperfine multiplets. The top right panel of Fig. 7 shows the hyperfine-splitting energy for the  $1S$  charmonium states:  $M_{1S,\text{hyp}} = M_{J/\psi} - M_{\eta_c}$ . It is found that there is a good agreement between two lattice results;

$113.4(9)(1)$  GeV from the NRp model with lattice inputs and  $113.8(8)$  GeV from the standard lattice spectroscopy. This simply suggests that there is no additional uncertainties induced by both determining the charmonium potential and the charm quark mass by the BS amplitude method and solving the nonrelativistic Schrödinger equation with them.

We remark that the values of the hyperfine-splitting are slightly smaller than the experimental one  $M_{1S,\text{hyp}}^{\text{exp}} = 116.6(1.2)$  GeV. This would be simply due to insufficient calibration of the RHQ parameters and also other possible systematic uncertainties including the remnant discretization artifact. On the other hand, the hyperfine splitting energy for the  $2S$  charmonium states, which is plotted in the bottom left panel of Fig. 7, shows that the value of  $M_{\psi'(2S)} - M_{\eta_c(2S)} = 41(6)(3)$  MeV obtained from the hybrid approach is roughly consistent with the experimental value  $47(1)$  MeV, within its error range.

The bottom right panel of Fig. 7 shows the  $1P$  hyperfine mass splitting which is given by an energy difference between the  $h_c$  and spin-averaged  $\chi_{cJ}$  states:  $M_{1P,\text{hyp}} = M_{\overline{\chi_{cJ}}} - M_{h_c}$ . Experimentally, the

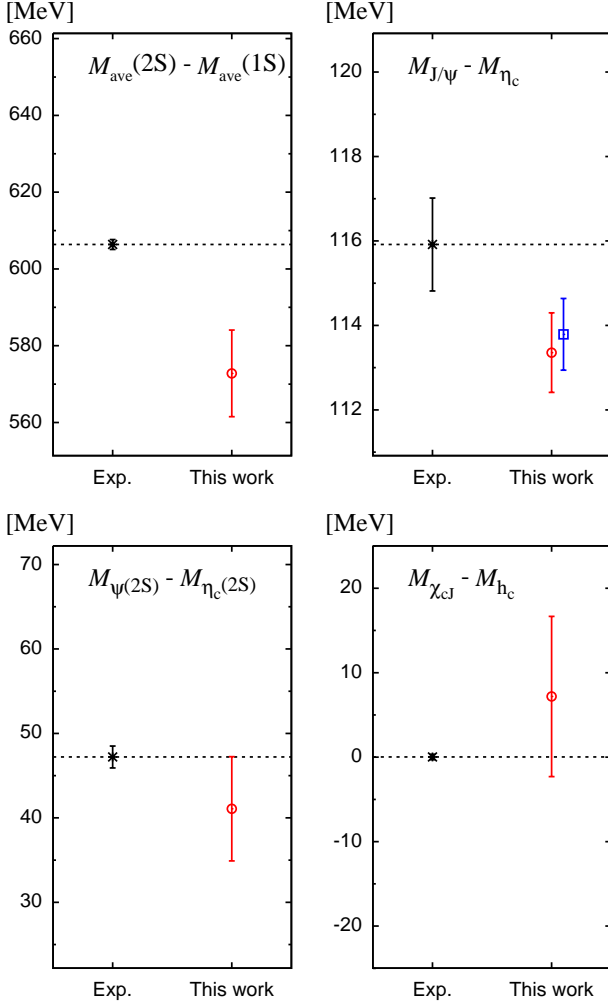


FIG. 7: Mass splittings of states lying below the open charm threshold in units of MeV, compared to the physical mass splitting. Upper panels show the mass splitting  $M_{\text{ave}}(2S) - M_{\text{ave}}(1S)$  between the spin-averaged  $1S$ - and  $2S$ -states (left), and the hyperfine mass splittings  $M_{J/\psi} - M_{\eta_c}$  between  $1S$ -states (right), while lower panels show mass splitting of  $M_{\psi(2S)} - M_{\eta_c(2S)}$  between  $2S$ -states (left) and mass splitting of  $M_{\chi_{cJ}} - M_{h_c}$  between  $1P$ -states (right). In each plot, cross and circle symbols indicate the experimental data and theoretical results obtained from the NRp model with the lattice inputs, respectively. The quoted errors indicate the sum of the statistical and systematic errors added in quadrature. Dashed lines represent the central value of the experiment. Only for the hyperfine mass splitting between  $1S$ -states, the results of the lattice spectroscopy is shown as a square.

value of  $M_{1P,\text{hyp}}^{\text{exp}}$  is known to be zero with high accuracy as  $M_{1P,\text{hyp}}^{\text{exp}} = 0.02(23)$  MeV [62, 63]. The hybrid approach yields a small splitting energy as  $M_{1P,\text{hyp}} = 7.2(1.6)(9.3)$  MeV, which is consistent with the zero value within a large error. Of course, however, the spin-spin charmonium potential determined in the BS amplitude method is not still enough to describe the tiny  $1P$  hyper-

fine splitting measured in experiment. As we mentioned in the previous subsection, a finite-range spin-spin potential gives a nonzero value of hyperfine mass splitting even in the case of higher-wave states such as  $P$ -wave state, while zero hyperfine splitting measured in experiments is easily reproduced by the *point-like* spin-spin potential widely adopted in phenomenological quark potential models. Here, we stress that the spin-spin potential from the BS amplitude method is *finite-range* and therefore the value of  $M_{1P,\text{hyp}}^{\text{exp}}$  is highly sensitive to both shapes of the spin-spin potential and wave functions of  $P$ -wave states. According to our systematic study of the BS amplitude method performed in quenched lattice QCD [21], the spin-spin potential receives large uncertainties due to the discretization artifacts more than the spin-independent central potential. To make a firm conclusion, it is necessary to perform the present calculation on the finer lattice.

Our theoretical calculations for the charmonium mass spectrum below the open-charm threshold are basically in good agreement with the experimental measurements. The point we wish to emphasize here is that our novel approach has no free parameters in solving the Schrödinger equation in contrast to the phenomenological NRp models. All of the parameters are fixed by lattice QCD simulations, where three light hadron masses (*e.g.* pion, kaon and  $\Omega$  baryon) are used for setting the lattice spacing  $a$  and hopping parameters of the light and strange quarks (*i.e.* the light and strange quark masses). In this study, the charm quark was treated in the quenched approximation. Then the experimental values of  $\eta_c$  and  $J/\psi$  charmonium masses are used to determine the charm quark parameters appeared in the RHQ action. In this sense, the hybrid approach proposed here is distinctly different from existing calculations in the phenomenological quark potential models.

Let us now attempt to straightforwardly extend the hybrid approach to above the open-charm threshold. Only the spin-averaged mass is considered for the  $P$  and  $D$  spin-triplet states:  $M(\overline{n^3P_J}) = (M_{n^3P_0} + 3M_{n^3P_1} + 5M_{n^3P_2})/9$  and  $M(\overline{n^3D_J}) = (3M_{n^3D_1} + 5M_{n^3D_2} + 7M_{n^3D_3})/15$ . In order to provide mass splittings among these spin-triplet states, the tensor and spin-orbit potentials are inevitably required. Since, in this paper, we succeeded in extracting the spin-spin potential solely for the spin-dependent potentials, we should focus on the spin-averaged masses.

First of all, one can observe that the values obtained from the hybrid approach above the open-charm threshold fairly agree with the existing experimental data, although errors are relatively large as shown in Table VI. We, however, are not in a position to give a realistic description to the higher-lying charmonium states, which are located above the open-charm threshold. This is because there are the following remarks in our calculations including the higher-lying charmonium states.

1. The higher-lying charmonium states significantly

suffer from systematic uncertainties, which are mainly due to the less knowledge of the long-range part of the spin-independent potential. We have no reasonable data for the charmonium potential at longer distances than about 1.1 fm since the wave function of the  $1S$  ground-state possesses the highly localized nature. Therefore we need to calculate the potential form the higher-lying charmonium states. Alternatively, we simply extrapolate the long-range behavior of the potential outside the region, where the charmonium potential is really determined from the localized wave function. In the latter case, the higher-lying spectrum of the charmonium is more sensitive to the choice of the adopted functional form in the fitting procedure.

2. The possible mass shift due to mixing the  $Q\bar{Q}$  states with  $D\bar{D}$  continuum is completely neglected in this study. One may expect that the NRp models without such mixing works well to describe the low-lying charmonium systems far below its threshold. On the other hand, such coupled channel effects might not be negligible near and above the threshold and then the potential description may lose the accuracy of theoretical prediction, though the naive treatment of the NRp models even for higher-lying charmonium states was phenomenologically successful despite the absence of coupled channel effects [3, 4]
3. For the higher-lying excitations of the spin-1 charmonium state, the  $S$ - $D$  mixing becomes severe since the level spacings between  $(n+1)^3S_1$  and  $n^3D_1$  get narrower [77]. However,  $S$ - $D$  mixing effects on  $J/\psi$ ,  $\psi(2S)$  and  $\psi(3S)$  states are not taken into account in the present calculation since the tensor term in the spin-dependent potentials is not determined in this study. Similarly, the mass estimations of  $\bar{\chi}_{c\bar{J}}(nP)$  and  $\bar{\psi}(nD)$  tabulated in Table VI are calculated without consideration of possible partial-wave mixings such as  $S$ - $D$ ,  $F$ - $P$  and  $D$ - $G$  mixings.

To calculate the BS wave function of  $1P$ -states, better source operators with respect to odd-parity wave function [78] are required. Meanwhile some extension of the variational method [79, 80] to the four-point correlation functions is necessary for extracting the BS wave function of the radial excitation of the  $S$ -wave states. These new calculations can give more realistic prediction especially to the higher-lying charmonia. The former provides information of the spin-orbit and also tensor potentials [78]. The latter can provide not only the tensor potential, but also the mixing angle between  $2^3S_1$  and  $1^3D_1$  states in the same way as the nuclear force [25]. Furthermore more data points of the charmonium potential at large distances can be accessible from such excited states of the charmonium, which have more extended wave function than that of  $1S$  ground states. Such kind of studies is now under way [81].

TABLE VII: Masses of low-lying  $D_s$  meson states, the spin-averaged mass and hyperfine splitting energy of  $1S$  charmonium states. The columns have the same meaning as in Table VI. Results are given in units of GeV.

state	$(J^P)$	$\Gamma$	fit range	mass [GeV]	$\chi^2/\text{d.o.f.}$
$D_s$	$(0^-)$	$\gamma_5$	[30:47]	1.9780(12)	1.08
$D_s^*$	$(1^-)$	$\gamma_i$	[30:47]	2.1230(42)	0.61
$M_{\text{ave}}(1S)$	—	—	—	2.0865(33)	—
$E_{\text{hyp}}(1S)$	—	—	—	0.1461(37)	—
$D_{s0}^*$	$(0^+)$	1	[14:26]	2.3536(77)	1.45
$D_{s1}$	$(1^+)$	$\gamma_5\gamma_i$	[14:26]	2.4689(83)	1.14
$D_{s1}$	$(1^+)$	$\gamma_i\gamma_j$	[14:22]	2.4893(87)	1.20

## VI. APPLICATION TO HEAVY-LIGHT SYSTEM

In the charmonium (heavy-heavy) system, the spectrum below the open charm threshold are well described by *potential description* with our charmonium potential including the spin-spin interaction, which was determined by the BS amplitude method in dynamical lattice QCD simulations. In this section, we apply the new method to the  $D_s$  heavy-light meson system, which represents the case of mesons with non-degenerate quark masses. Apart from the phenomenological interest, we also would like to examine the validity range of the new method in terms of the size of quark kinetic mass.

### A. Lattice setup for charmed-strange mesons

The numerical setup for the charmed-strange ( $D_s$ ) mesons system is basically same as for the calculation of the charmonium system. For the charm quark, we use the RHQ action with the parameters calibrated by  $1S$ -charmonium states. In addition to the computation of the charm quark propagator, another fermion matrix inversion for a strange quark is required to compute the  $D_s$ -meson correlation functions. The non-perturbatively  $\mathcal{O}(a)$ -improved Wilson quark action ( $c_{SW} = 1.715$ ) is used for the strange quark. A hopping parameter of the strange quark is chosen to be  $\kappa_s = 0.13640$ , which is the same as the sea strange quark used in gauge field generation. Simultaneously,  $s\bar{s}$ -mesons are supplementarily calculated, and we use  $s\bar{s}$ -meson data for a consistency check on the kinetic masses of the strange quark determined through  $s\bar{s}$  and  $c\bar{s}$  systems as we will discuss later.

Fig. 8 shows the effective mass plots for  $S$  and  $P$ -wave  $D_s$ -meson states. The  $D_s$ -meson masses are determined by constant fits to the plateaus observed in the effective mass plots with covariance matrices accounting for the data correlation among different time slices. Results of the  $D_s$ -meson masses together with fit ranges used in the fits and the values of  $\chi^2/\text{d.o.f.}$  are summarized in Table VII. The quoted errors represent only the statistical errors given by the jackknife analysis. The

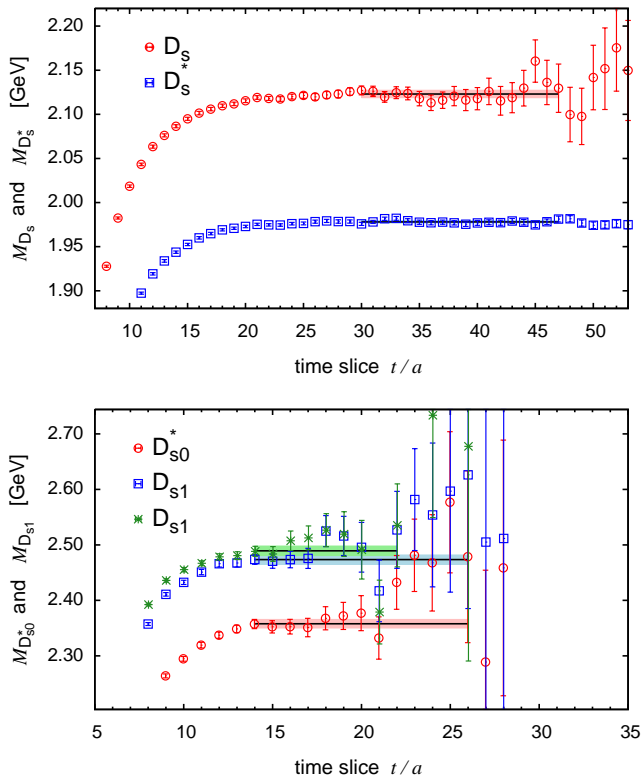


FIG. 8: Effective mass plots for low-lying  $S$  and  $P$ -wave  $D_s$  meson states.  $S$ -wave states ( $D_s$  and  $D_s^*$ ) and  $P$ -wave states ( $D_{s0}^*(2317)$ ,  $D_{s1}(2460)$  and  $D_{s1}(2536)$ ) are shown in the upper and lower panels, respectively. Each  $D_s$  meson state is specified in legend. Horizontal lines and shaded bands denote fit results with statistical errors estimated by the jackknife method and their fit range.

RHQ action for the charm quark works well even for the low-lying  $D_s$ -mesons. The spin-averaged and hyperfine splitting  $D_s$ -meson masses,  $M_{\text{ave}}^{1S} = 2.0865(33)$  GeV and  $M_{\text{hyp}}^{1S} = 0.1461(37)$  GeV, are obtained from the standard lattice spectroscopy. Although the simulated strange quarks are slightly off the physical point, these results are quite close to the experimental data of  $M_{\text{ave}}^{\text{exp}}(1S) = 2.07635(27)$  GeV and  $M_{\text{hyp}}^{\text{exp}}(1S) = 0.1438(4)$  GeV. The deviations from the experimental results are within about 0.5%. Furthermore, results of  $P$ -wave  $D_s$ -meson states from the lattice spectroscopy marginally reproduce the experimental data. Similar results are reported by the PACS-CS collaboration using  $2 + 1$  flavor dynamical gauge configurations generated with the physical strange quark [44, 82].

The two-point correlation functions of both pseudoscalar and vector  $s\bar{s}$ -mesons, *i.e.*  $\eta_{s\bar{s}}(0^-)$  and  $\phi(1^-)$  mesons, are also calculated in this study. We obtain results of  $M_{\eta_{s\bar{s}}} = 0.7699(9)$  GeV and  $M_\phi = 1.0827(68)$  GeV. The similar values are reported in Ref. [22]. The fit range was chosen to be  $24 \leq t \leq 39$  for both states. The  $\phi$  meson mass is somewhat heavier than the experimental values of  $M_\phi^{\text{exp}} =$

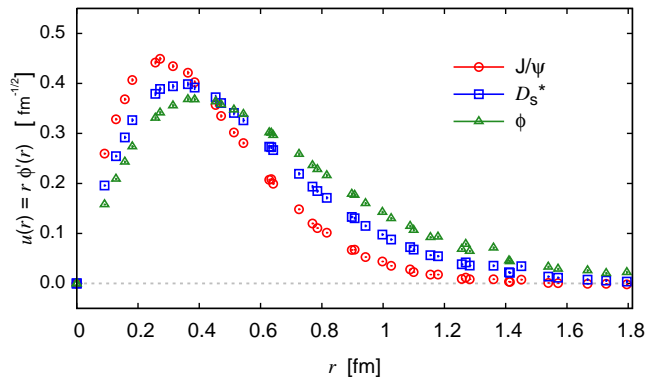


FIG. 9: The reduced BS wave function  $u(r) = r\phi(r)$  for the  $1S$  vector  $c\bar{c}$  (circles),  $c\bar{s}$  (squares) and  $s\bar{s}$  (triangles) states, as a function of spatial distance  $r$ . They are normalized as  $\sum \phi(\vec{x}) = 1$ .

1.019455(20) GeV. It should be attributed to the fact that the simulated strange quarks are slightly off the physical point. Although the systematic uncertainty due to slightly heavier strange quark mass is expected to be extremely small in the charmonium spectrum, we should take into account some corrections for the  $D_s$ -meson spectrum [46].

## B. BS wave function

In Fig. 9, we show the reduced BS wave functions for the  $1S$  vector  $c\bar{c}$ ,  $c\bar{s}$  and  $s\bar{s}$  states corresponding to  $J/\psi$ ,  $D_s^*$  and  $\phi$  mesons, respectively. It is found that the  $D_s^*$  wave function is spatially extended to at least the half of the spatial extent of lattice volume ( $N_s a/2 \sim 1.5$  fm). Although the amplitude of the wave function of the  $D_s^*$  meson is considerably small at  $r \sim 1.5$  fm, it still seems to remain non-zero values in the range of  $r > 1.5$  fm, where only off-axis data points are available. The wrap round effect would cause the rotational symmetry breaking at longer distances. Therefore, in the  $D_s$  system, the interquark potential could be more affected by the finite volume effect than the charmonium system. In the case of the  $s\bar{s}$  system, which is more spatially extended than the  $c\bar{s}$  system as shown in Fig. 9, this problem could become more severe.

## C. quark kinetic mass

Fig. 10 illustrates the determination of quark kinetic mass from the  $c\bar{s}$  and  $s\bar{s}$  meson systems in the BS amplitude method. A quantity  $m_{Qq}$  is defined as twice the reduced mass of the  $D_s(c\bar{s})$  system:  $m_{Qq} = 2m_Q m_q / (m_Q + m_q)$ , while  $m_q$  corresponds to the strange quark mass.

As shown in the upper panel of Fig. 10, we fit the data points of the  $c\bar{s}$  meson system at relatively large



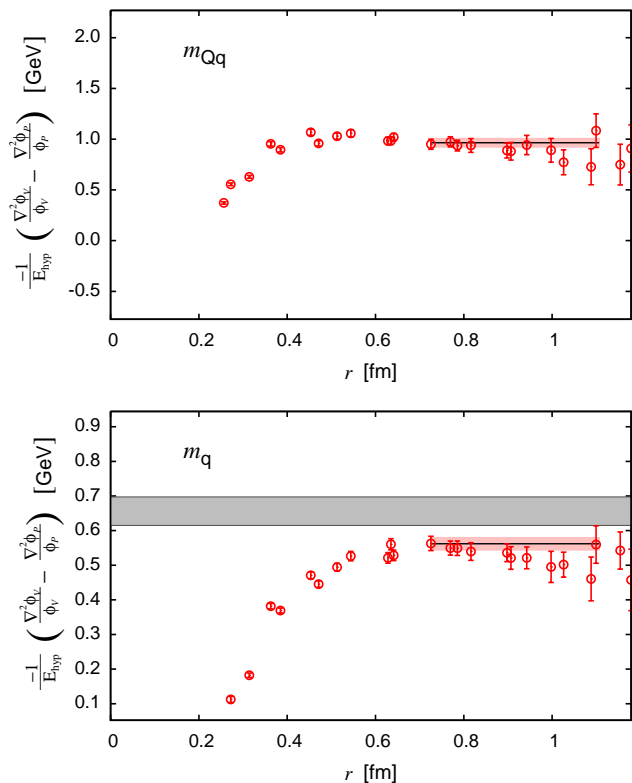


FIG. 10: The determination of the reduced mass  $m_{Qq}$  from the  $D_s(c\bar{s})$  system (upper) and strange quark mass  $m_q$  from the  $s\bar{s}$  system (lower) in the BS amplitude method. We obtain the quark kinetic masses of  $m_{Qq}$  and  $m_q$  from the asymptotic behavior of the right-hand side of Eq. (8) in long-distance region. Solid lines with shaded bands represent the fitting results and fit ranges with the statistical error estimated by the jackknife method. In the lower plot, a horizontal shaded band indicates a kinetic mass of the strange quark, which is independently evaluated by the relation  $m_q = m_{Qq}m_Q/(2m_Q - m_{Qq})$  with the values of  $m_{Qq}$  and  $m_Q$  from the  $c\bar{s}$  and  $c\bar{c}$  systems.

distances, where the reasonable plateau is found in the region of  $r \gtrsim 0.7$  fm. We then obtain the value of  $m_{Qq} = 0.959(45)(34)(36)$  GeV. The first error is statistical, and the second and third ones are systematic uncertainties due to the choice of data points taken from three directions and a variation of  $t_{\min}$ , respectively. The strange quark mass  $m_q$  can be evaluated by two data sets of  $m_{Qq}$  and  $m_Q$  through the relation  $m_q = m_{Qq}m_Q/(2m_Q - m_{Qq})$ . The value of  $m_Q$  corresponds to the charm mass, which was already determined in the previous section. When combined with results obtained from the  $D_s(c\bar{s})$  and charmonium ( $c\bar{c}$ ) system, we obtain the value of  $m_q = 656(41)$  MeV for the strange quark mass. Quoted error is statistical one, which was determined by the jackknife method.

Independently, the strange quark mass  $m_q$  can be determined through the  $s\bar{s}$  system as depicted by circle symbols in the lower panel of Fig. 10. Similar to the

TABLE VIII: Charm and strange quark masses, which are determined from the Coulomb-gauge quark-antiquark BS amplitude and the Landau-gauge quark propagator, are summarized in units of GeV.

flavor	BS amplitude		quark propagator
	$Q\bar{Q}$ or $q\bar{q}$	$Q\bar{q}$	Landau gauge
charm	1.784(23)	—	1.776(8)
strange	0.554(19)	0.656(41)	0.643(5)

upper figure, the reasonable plateau is found in the region of  $r \gtrsim 0.7$  fm. We compute a weighted average of the data points in the range of  $8 \leq r/a \leq 7\sqrt{3}$  with a covariance matrix accounting for the correlation, and then obtain the value of  $m_q = 554(19)(6)(8)$  MeV, which is close to a typical value of constituent strange quark mass ( $\sim M_\phi/2 \approx 500$  MeV) adopted in  $SU(6)$  quark models [1]. The meaning of the three quoted errors is explained above.

For comparison, the previously estimated value of  $m_q = 656(41)$  MeV from the data sets of  $m_{Qq}$  and  $m_Q$  is also displayed by a horizontal shaded band in the lower figure. There is  $2\sigma$  discrepancy between this band and the plateau behavior of  $-(\nabla^2\phi_V/\phi_V - \nabla^2\phi_{PS}/\phi_{PS})/E_{\text{hyp}}$  for the  $s\bar{s}$  system at large distances. Although this discrepancy may imply that nonrelativistic treatment is no longer valid for the heavy-light system, we would like to remind of the fact that the BS wave function of the  $s\bar{s}$ -meson system at large distances is likely affected by the finite volume effect as discussed previously.

The following discussion shows that the above speculation is likely to be true. The strange quark mass determined from the BS wave function of the  $s\bar{s}$ -meson states is indeed underestimated compared to a “pole mass” determined from the effective mass of gauge-variant quark two-point correlator *in the Landau gauge*, while two different calculations show remarkable consistency for the charm quark as summarized in Table VIII. Fig. 11 shows effective mass plots and comparisons with ones obtained within the BS amplitude method. The Landau-gauge pole mass is an alternative way of measuring the quark mass in lattice QCD. For details of how to calculate it, see Ref. [83].

If one may choose the  $c\bar{s}$  result rather than the  $s\bar{s}$  result for the BS amplitude method, the strange quark masses from two estimation methods become consistent again. Although the physics behind the consistency discussed here is beyond the scope of this paper, we may simply conclude that the discrepancy between results from the  $c\bar{s}$  and  $s\bar{s}$  mesons is mainly attributed to the finite volume effect on the  $s\bar{s}$  wave function.

#### D. charmed-strange potential

Fig 12 shows results of the spin-independent and spin-spin interquark potentials obtained from the  $D_s$  and  $D_s^*$

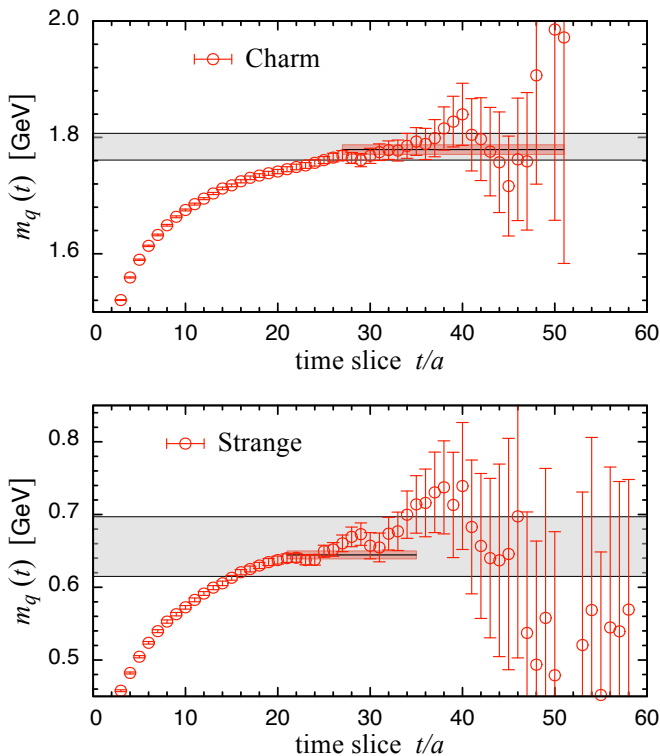


FIG. 11: Effective masses of gauge-variant quark two-point correlator in the Landau gauge for charm (upper panel) and strange (lower panel). Solid lines indicate fit results for “pole” masses of charm and strange quarks and shaded bands display the fitting ranges and one standard deviations estimated by the jackknife method. In each panel, a wider and horizontal shaded band indicates a kinetic mass evaluated from the  $c\bar{s}$  and/or  $c\bar{c}$  systems within the BS amplitude method.

meson states (hereafter called  $c\bar{s}$  potential) in the dynamical QCD simulation. For purpose of comparison, the charmonium potentials are also displayed.

At first glance, a shape of the  $c\bar{s}$  potential is basically similar to that of the charmonium potential, so that we similarly adopt the Cornell potential form for the spin-independent  $c\bar{s}$  potential and also exponential (Yukawa) form for the spin-spin  $c\bar{s}$  potential as is the case in the charmonium potential. We obtain the Cornell parameters of the  $c\bar{s}$  potential as  $A = 1.30(8)(22)(21)(21)$  and  $\sqrt{\sigma} = 324(16)(34)(26)(4)$  MeV with a reasonably small value of  $\chi^2/\text{d.o.f.} \approx 1.9$ . The first error is statistical and the second, third and fourth ones are systematic uncertainties due to the choice of data points taken from three directions, and variations of  $t_{\min}$  and  $r_{\min}$ , respectively.

The appropriate fitting range was determined to minimize a  $\chi^2/\text{d.o.f.}$  value taking into account the data correlation among different spatial distances  $r$ . We choose the fit range of  $[r_{\min}/a : r_{\max}/a] = [4 : 7\sqrt{3}]$ , which corresponds to the same range in the case of the charmonium potential. Although the string tension has weak dependence on quark kinetic mass [21], the Coulomb coefficient of the  $c\bar{s}$  potential significantly grows in com-

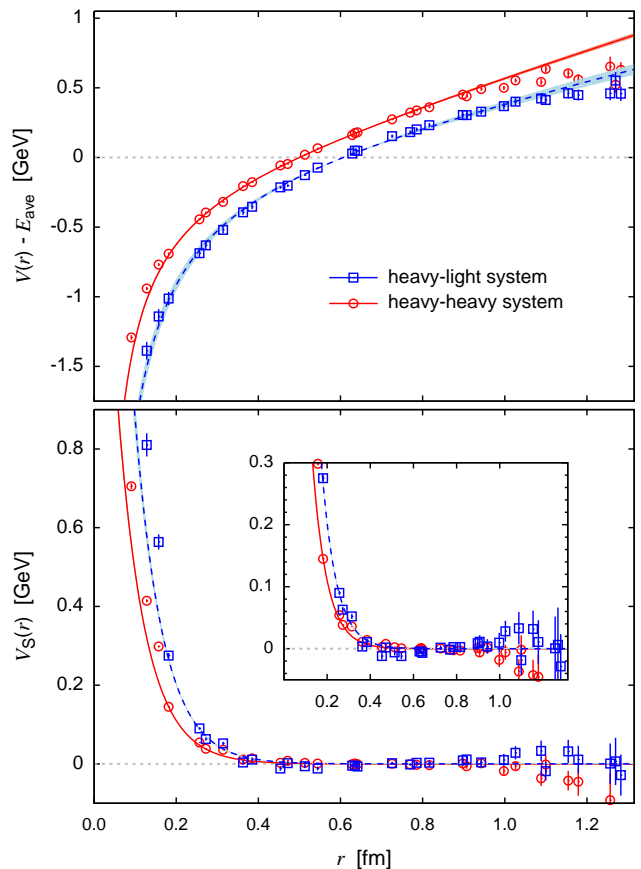


FIG. 12: The spin-independent and spin-spin interquark potentials for the  $c\bar{c}$  (circles) and  $c\bar{s}$  (squares) systems, calculated from the BS wave functions in dynamical lattice QCD simulations with almost physical quark masses. In the upper panel, the spin-independent parts of both the charmonium and  $c\bar{s}$  potentials are plotted. For clarity of the figure, the constant energy shift  $E_{\text{ave}}$ , which is given by the spin-averaged mass of  $1S$  states, is not subtracted. Solid and dashed curves represent the fit results with the Cornell parametrization. The shaded bands show statistical uncertainties in the fitting procedure where the jackknife method is employed. In the lower panel, we show the spin-spin potential  $V_S(r)$ . The exponential form is used for fitting the resultant spin-spin potentials for the  $c\bar{c}$  and  $c\bar{s}$  systems. The inset shows a magnified view.

parison with that of the charmonium potential. For the spin-spin potential, we obtain  $\alpha = 3.79(36)$  GeV and  $\beta = 2.89(9)$  GeV ( $\alpha = 1.48(14)$  and  $\beta = 1.97(9)$  GeV) from the exponential (Yukawa) form fit with  $\chi^2/\text{d.o.f.} \approx 1.49$  ( $\chi^2/\text{d.o.f.} \approx 1.86$ ). We quote only the statistical errors, which are determined by the jackknife method. We find that the size of the finite-range of the spin-spin potential for the  $c\bar{s}$  system is almost consistent with the one obtained from the charmonium spin-spin potential within statistical uncertainties.

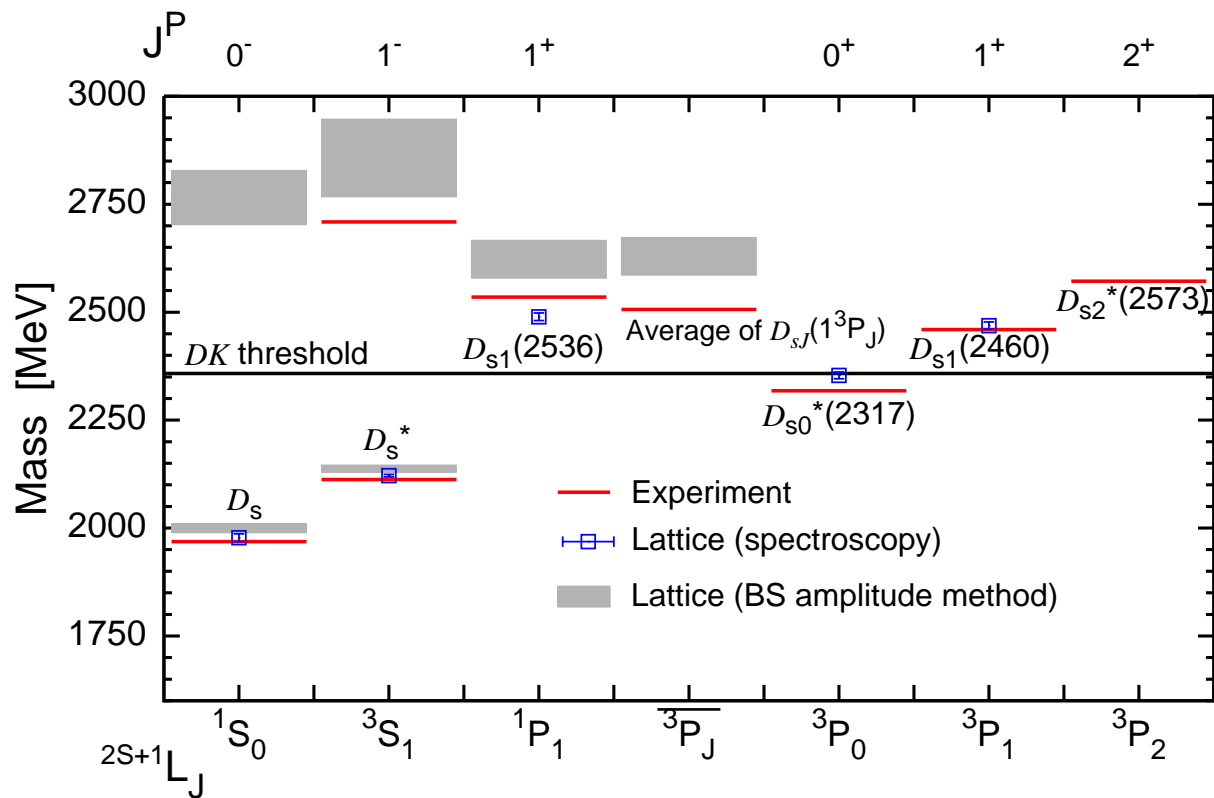


FIG. 13: Mass spectrum of the charmed-strange mesons around the  $DK$  threshold. The vertical scale is in units of MeV. Labels of  $^{2S+1}[L]_J (J^P)$  are displayed in lower (upper) horizontal axis. Solid lines indicate experimental values of well established  $D_s$  meson states, while square symbols represent results of the standard lattice spectroscopy. Rectangular shaded boxes indicate predictions from the NRp models with purely theoretical inputs based on lattice QCD and their errors which are the sum of the statistical and systematic errors added in quadrature. A horizontal solid line shows the  $DK$  threshold. A symbol of  $^3\overline{P}_J$  denotes the spin-weighted average of spin-triplet  $^3P_J$  states.

### E. charmed-strange meson mass spectrum

Using the  $c\bar{s}$  potential calculated from lattice QCD, we obtain the spectrum of the charmed-strange mesons in the same footing as the charmonium spectrum discussed in Sec. V C. The resulting  $D_s$  meson spectrum together with the experimental values and the results from the standard lattice spectroscopy are summarized in Table IX and also Fig. 13.

The results of  $1S$  states in the  $D_s$ -meson family by solving the discrete nonrelativistic Schrödinger equation with lattice inputs show a good agreement with both experiments and standard lattice calculations below the  $DK$  threshold. Above the  $DK$  threshold, the  $c\bar{s}$  potential obtained from the BS amplitude method can properly reproduce the mass ordering of the  $D_s$  mesons, while absolute values of the masses are systematically larger than the experimental values; for example, the corresponding  $D_{s1}(2536)$  state is overestimated by about 90 MeV, and then observe a large systematic discrepancy between two kinds of lattice QCD results.

Recall that the results obtained from the standard lattice spectroscopy near the  $DK$  threshold are also slightly

deviated from the experimental values. Although this implies that the observed discrepancies among them are not solely attributed to the BS amplitude approach, there are three possible sources of above mentioned discrepancies in our method. The first is, as we have noted repeatedly, associated with uncertainties in the long-range part of the spin-independent potential. The fact that the  $D_s$  state has the wider wave function leads to the large finite volume effect on the interquark potential determined within the BS amplitude method at long distances. Furthermore, information of the  $c\bar{s}$  potential is accessible only within the “size” of the  $S$ -wave  $D_s$  mesons. We therefore force the wave function to be zero at the spatial boundary in the process of solving the discrete nonrelativistic Schrödinger equation with present limited data of the  $c\bar{s}$  potential.

The second possibility is that there are the  $DK$  and  $D^*K$  threshold effects. Since  $D_{s0}(2310)$  and  $D_{s1}(2460)$  are located near the  $DK$  and  $D^*K$  thresholds respectively. Therefore, the coupling of these states to the  $DK$  and  $D^*K$  two-hadron states could not be negligible [85, 86]. Such channel couplings may cause level repulsion and thus mass shift by the threshold effect might

TABLE IX: Masses of low-lying  $D_s$  mesons are summarized in units of MeV. The labels of AVE and HYP in a column of “state” for  $S$ -wave states denotes the spin-averaged mass  $(M_{1S_0} + 3M_{3S_1})/4$  and hyperfine splitting mass  $M_{3S_1} - M_{1S_0}$ . Experimental values in the second column are taken from Particle Data Group, rounded to 1 MeV [45]. There are two kinds of lattice QCD results tabulated in the third and fourth columns. One is obtained by the standard lattice spectroscopy, while another is evaluated by solving the Schrödinger equation with the  $c\bar{s}$  potential determined from lattice QCD. For the latter, the first error is statistical and the second error systematic as described in text. The spin-weighted average mass (denoted as  ${}^3[L]_J$ ) are also included for spin triplet states  ${}^3[L]_J$ . The last column gives the results from a NRp model [84].

state	Exp.	Lattice QCD (This work)		NRp model [84]
		spectroscopy	BS amplitude	
$D_s (1^1S_0)$	1968	1978(1)	2000(10)(3)	1963
$D_s^* (1^3S_1)$	2112	2123(4)	2138(8)(3)	2099
AVE	2076	2087(3)	2103(8)(3)	2065
HYP	144	146(4)	138(5)(1)	136
$D_s (2^1S_0)$			2766(38)(50)	
$D_s^* (2^3S_1)$	2709		2857(42)(80)	
AVE			2834(40)(73)	
HYP			92(9)(30)	
$D_{s1} (1^1P_1)$	2535	2489(9)	2623(30)(32)	2527
$D_{sJ} (1^3P_J)$	2506		2629(29)(32)	2532
$D_{s0}^* (1^3P_0)$	2318	2354(8)		2446
$D_{s1} (1^3P_1)$	2460	2469(8)		2515
$D_{s2}^* (1^3P_2)$	2572			2561

be happened [87–89].

Finally, it is worth pointing out that we assumed that there is no  $S$ - $D$  mixing due to the tensor force because of large energy gap between  $1S$  and  $1D$  states. Strictly speaking, however, the  $D_s^*$  meson which is specified by the quantum numbers  $J^P = 1^-$  is not purely composed of the  ${}^3S_1$  wave function. This approximation could introduce a small correction to the intermediate and short-range parts of the  $c\bar{s}$  potential calculated in the BS amplitude method.

Therefore, we need further development of our approach to take into account both the coupled channel effect and  $S$ - $D$  mixing. A simulation with sufficiently large volume is also required for precise prediction of masses of the  $D_s$ -meson states near and above the  $DK$  ( $D^*K$ ) threshold within our approach.

## VII. SUMMARY

We have calculated the interquark potentials for both the charmonium ( $c\bar{c}$ ) and charmed-strange ( $c\bar{s}$ ) mesons at almost physical point. The interquark potential with finite quark masses are defined through the equal-time Bethe-Salpeter wave functions of the pseudoscalar and vector mesons. Our simulations have been done in the

vicinity of the physical light quark masses, which corresponds to  $M_\pi \approx 156$  MeV, using the PACS-CS Iwasaki gauge configurations with 2+1 flavors of dynamical clover light quarks. We use the relativistic charm quark tuned to reproduce the experimental values of the  $\eta_c$  and  $J/\psi$  masses.

We first investigated the charmonium potential. The resulting spin-independent potential has the Coulomb-plus-linear form, and their parameters are close to the values used in the phenomenological NRp models. The string breaking due to the presence of dynamical sea quarks is not apparently observed. The spin-spin potential obtained from the dynamical simulations exhibits the finite-range repulsive interaction. Its shape is quite different from a repulsive  $\delta$ -function potential induced by the one-gluon exchange, which is often adopted in the NRp models.

Our ultimate goal is to reveal the mystery behind rich structures recently observed in the heavy-heavy and heavy-light systems including the newly discovered charmonium-like mesons. As a first step, we calculated the charmonium mass spectrum by solving nonrelativistic Schrödinger equation with purely theoretical inputs of the spin-independent and spin-spin potentials, and also the quark kinetic mass. To avoid any model dependence from fitting, we practically solve the discrete Schrödinger equation in finite volume with Dirichlet boundary condition, and thus can handle direct lattice data of the charmonium potential without any parameterization.

We found an excellent agreement of low-lying charmonium masses between our results and the experimental data. We here emphasize that our novel approach has no free parameters in solving the Schrödinger equation in contrast to the phenomenological NRp models. In our calculations, three light hadron masses (*e.g.* the pion, kaon and  $\Omega$  baryon are chosen in the PACS-CS collaboration) and two charmonium masses (the  $\eta_c$  and  $J/\psi$ ) are used for fixing the lattice spacing and quark mass parameters in the lattice QCD action including the RHQ parameters for the charm quarks.

In order to precisely predict the mass spectrum above the open charm threshold, we should take into account both coupled-channel effect with the  $D\bar{D}$  continuum and  $S$ - $D$  mixing due to the presence of the tensor force. In this study, we simply ignore these effects and then apply the hybrid approach to higher-lying charmonium states above the open-charm threshold. We found that the theoretical predictions of the NRp model calculation with lattice inputs are remarkably consistent with well-established experimental data for the conventional charmonium states.

For an application, we straightforwardly extend our method to calculate the charmed-strange meson system, which represents the case of mesons with non-degenerate quark masses and also heavy-light system. A shape of the interquark  $c\bar{s}$  potential in the  $D_s$ -meson system is basically similar to that of the charmonium potential. Using the resulting  $c\bar{s}$  potential as theoretical inputs, we obtain

the spectrum of the charmed-strange mesons. Below the  $DK$  threshold, our new method works well in spite of the fact that the  $D_s$  mesons contain a strange quark or strange anti-quark. Although above the  $DK$  threshold our  $c\bar{s}$  potential can reproduce the mass ordering of the  $D_s$  mesons, absolute values of the masses are consistent with neither the experimental values nor the results from the standard lattice spectroscopy.

Although it is difficult to draw any firm conclusion at this stage, the discrepancies observed above the  $DK$  threshold suggest that all of coupled-channel effect,  $S$ - $D$  mixing and higher-order relativistic corrections, that are omitted in this study, are possibly important to understand the properties of the heavy-light mesons near the threshold. To disentangle these effects, simulations in a larger lattice is necessary. Conversely, one might say that by taking into account these effects properly, our approach can give a systematic way to examine the validity of the potential description even for the charmed-strange system. Such full analysis finally sheds light on the detailed properties of the  $D_s$  mesons.

At least, in this study, the charmonium and charmed-strange potentials obtained from the BS amplitude method have been succeed in reproducing the low-lying masses below the open charm threshold and  $DK$  threshold respectively. Furthermore we showed that our new analysis can potentially shed light on the detailed properties of the heavy quarkonium system. While only energy eigenvalues are evaluated from temporal information of meson correlation functions in the standard lattice spectroscopy, the new method takes an advantage of full spatial information together with temporal information. The BS wave functions can be identified with the eigenstates of the Hamiltonian. Hence, without knowing the details of an explicit form of the Hamiltonian, lots of physical quantities could be calculated directly by the BS wave functions as studied in the NRp models. For examples,  $E1$  and  $M1$  radiative partial widths are supposed

to be evaluated with the BS wave functions of the charmonium states. Such information is important to reveal the structure of hadrons.

To derive a complete nonrelativistic Hamiltonian of the heavy-heavy and heavy-light systems from lattice QCD, we must calculate all spin-dependent terms (spin-spin, tensor and spin-orbit forces), which are required for more realistic predictions for the higher-lying states. We now develop the BS amplitude method to calculate the BS wave functions of  $P$ -wave mesons, which provides information of the spin-orbit and also tensor potentials.

Once all spin-dependent terms of the interquark potential are determined and also all systematic uncertainties are well understood, we will gain new and valuable insight on the mesons newly discovered in the heavy-heavy and heavy-light systems. It is also important to examine the validity of the potential description with the BS amplitude method from the viewpoint of the  $v$ -expansion for a nonlocal and energy-independent interquark potential  $U$  originally appeared in Eq. (4). For this purpose, we would like to examine whether the same interquark potential is obtained from the BS wave function of the radial excitation of the  $S$ -wave states. All of the above-mentioned extensions of the new method are now in progress [81].

#### Acknowledgments

We would like to thank T. Hatsuda for helpful suggestions, H. Iida, Y. Ikeda and B. Charron for fruitful discussions. This work was partially supported by JSPS/MEXT Grants-in-Aid (No. 22-7653, No. 19540265, No. 21105504 and No. 23540284). T. Kawanai was partially supported by JSPS Strategic Young Researcher Overseas Visits Program for Accelerating Brain Circulation (No.R2411).

- 
- [1] F. Close, *An introduction to quarks and partons*, Academic Press/London 1979, 481p.
  - [2] E. Eichten, K. Gottfried, T. Kinoshita, J. B. Kogut, K. Lane, et al., Phys.Rev.Lett. **34**, 369 (1975).
  - [3] S. Godfrey and N. Isgur, Phys.Rev. **D32**, 189 (1985).
  - [4] T. Barnes, S. Godfrey, and E. Swanson, Phys.Rev. **D72**, 054026 (2005), hep-ph/0505002.
  - [5] E. Eichten and F. Feinberg, Phys.Rev. **D23**, 2724 (1981).
  - [6] N. Brambilla, A. Pineda, J. Soto, and A. Vairo, Rev.Mod.Phys. **77**, 1423 (2005), hep-ph/0410047.
  - [7] M. Voloshin, Prog.Part.Nucl.Phys. **61**, 455 (2008), 0711.4556.
  - [8] A. Bondar et al. (Belle), Phys. Rev. Lett. **108**, 122001 (2012), 1110.2251.
  - [9] S. Godfrey and S. L. Olsen, Ann.Rev.Nucl.Part.Sci. **58**, 51 (2008), 0801.3867.
  - [10] F. J. Wegner, J. Math. Phys. **12**, 2259 (1971).
  - [11] K. G. Wilson, Phys.Rev. **D10**, 2445 (1974).
  - [12] G. S. Bali, Phys.Rept. **343**, 1 (2001), hep-ph/0001312.
  - [13] G. S. Bali, K. Schilling, and A. Wachter, Phys.Rev. **D55**, 5309 (1997), hep-lat/9611025.
  - [14] G. S. Bali, K. Schilling, and A. Wachter, Phys.Rev. **D56**, 2566 (1997), hep-lat/9703019.
  - [15] Y. Koike, Phys.Lett. **B216**, 184 (1989).
  - [16] K. Born, E. Laermann, T. Walsh, and P. Zerwas, Phys.Lett. **B329**, 332 (1994).
  - [17] Y. Koma and M. Koma, Nucl.Phys. **B769**, 79 (2007), hep-lat/0609078.
  - [18] Y. Koma and M. Koma, Prog.Theor.Phys.Suppl. **186**, 205 (2010).
  - [19] T. Kawanai and S. Sasaki, Phys.Rev.Lett. **107**, 091601 (2011), hep-lat/1102.3246.
  - [20] T. Kawanai and S. Sasaki, Phys.Rev. **D85**, 091503 (2012), 1110.0888.
  - [21] T. Kawanai and S. Sasaki, Phys. Rev. **D89**, 054507 (2014), 1311.1253.

- [22] S. Aoki et al. (PACS-CS Collaboration), *Phys.Rev.* **D79**, 034503 (2009), 0807.1661.
- [23] S. Aoki, Y. Kuramashi, and S.-i. Tominaga, *Prog.Theor.Phys.* **109**, 383 (2003), hep-lat/0107009.
- [24] N. Ishii, S. Aoki, and T. Hatsuda, *Phys.Rev.Lett.* **99**, 022001 (2007), nucl-th/0611096.
- [25] S. Aoki, T. Hatsuda, and N. Ishii, *Prog.Theor.Phys.* **123**, 89 (2010), 0909.5585.
- [26] H. Nemura, N. Ishii, S. Aoki, and T. Hatsuda, *Phys.Lett.* **B673**, 136 (2009), 0806.1094.
- [27] Y. Ikeda (HAL QCD Collaboration), *Prog.Theor.Phys.Suppl.* **186**, 228 (2010).
- [28] T. Kawanai and S. Sasaki, *Phys.Rev.* **D82**, 091501 (2010), 1009.3332.
- [29] T. Doi et al. (HAL QCD Collaboration), *Prog.Theor.Phys.* **127**, 723 (2012), 1106.2276.
- [30] S. Aoki et al. (HAL QCD Collaboration) (2012), 1206.5088.
- [31] K. Murano, N. Ishii, S. Aoki, and T. Hatsuda, *Prog.Theor.Phys.* **125**, 1225 (2011), 1103.0619.
- [32] S. Aoki et al. (HAL QCD Collaboration), *Proc.Japan Acad.* **B87**, 509 (2011), 1106.2281.
- [33] N. Ishii et al. (HAL QCD Collaboration), *Phys.Lett.* **B712**, 437 (2012), 1203.3642.
- [34] B. Velikson and D. Weingarten, *Nucl.Phys.* **B249**, 433 (1985).
- [35] R. Gupta, D. Daniel, and J. Grandy, *Phys.Rev.* **D48**, 3330 (1993), hep-lat/9304009.
- [36] M. Luscher, *Nucl.Phys.* **B354**, 531 (1991).
- [37] W. E. Caswell and G. P. Lepage, *Phys.Rev.* **A18**, 810 (1978).
- [38] Y. Ikeda and H. Iida (2011), 1102.2097.
- [39] S. Aoki et al. (CP-PACS Collaboration, JLQCD Collaboration), *Phys.Rev.* **D73**, 034501 (2006), hep-lat/0508031.
- [40] Y. Iwasaki (1983), 1111.7054.
- [41] Y. Kayaba et al. (CP-PACS Collaboration), *JHEP* **0702**, 019 (2007), hep-lat/0611033.
- [42] A. X. El-Khadra, A. S. Kronfeld, and P. B. Mackenzie, *Phys.Rev.* **D55**, 3933 (1997), hep-lat/9604004.
- [43] N. H. Christ, M. Li, and H.-W. Lin, *Phys.Rev.* **D76**, 074505 (2007), hep-lat/0608006.
- [44] Y. Namekawa et al. (PACS-CS Collaboration), *Phys.Rev.* **D84**, 074505 (2011), 1104.4600.
- [45] J. Beringer et al. (Particle Data Group), *Phys.Rev.* **D86**, 010001 (2012).
- [46] D. Mohler and R. Woloshyn, *Phys.Rev.* **D84**, 054505 (2011), 1103.5506.
- [47] C. McNeile and C. Michael (UKQCD Collaboration), *Phys.Rev.* **D70**, 034506 (2004), hep-lat/0402012.
- [48] P. de Forcrand et al. (QCD-TARO Collaboration), *JHEP* **0408**, 004 (2004), hep-lat/0404016.
- [49] L. Levkova and C. DeTar, *Phys.Rev.* **D83**, 074504 (2011), 1012.1837.
- [50] Y. Koma and M. Koma, *PoS LAT2009*, 122 (2009), 0911.3204.
- [51] A. Laschka, N. Kaiser, and W. Weise, *Phys.Lett.* **B715**, 190 (2012), 1205.3390.
- [52] Y. Koma, M. Koma, and H. Wittig, *Phys.Rev.Lett.* **97**, 122003 (2006), hep-lat/0607009.
- [53] S. Aoki et al. (CP-PACS Collaboration), *Nucl.Phys.Proc.Suppl.* **73**, 216 (1999), hep-lat/9809185.
- [54] G. S. Bali et al. (TXL Collaboration, T(X)L Collaboration), *Phys.Rev.* **D62**, 054503 (2000), hep-lat/0003012.
- [55] B. Bolder, T. Struckmann, G. S. Bali, N. Eicker, T. Lippert, et al., *Phys.Rev.* **D63**, 074504 (2001), hep-lat/0005018.
- [56] C. Bernard et al. (MILC Collaboration), *Nucl.Phys.Proc.Suppl.* **119**, 598 (2003), hep-lat/0209051.
- [57] P. Pennanen and C. Michael (UKQCD Collaboration) (2000), hep-lat/0001015.
- [58] C. W. Bernard, T. A. DeGrand, C. E. Detar, P. Lacey, S. A. Gottlieb, et al., *Phys.Rev.* **D64**, 074509 (2001), hep-lat/0103012.
- [59] G. S. Bali, H. Neff, T. Duessel, T. Lippert, and K. Schilling (SESAM Collaboration), *Phys.Rev.* **D71**, 114513 (2005), hep-lat/0505012.
- [60] C. E. Detar, O. Kaczmarek, F. Karsch, and E. Laermann, *Phys.Rev.* **D59**, 031501 (1999), hep-lat/9808028.
- [61] W. Buchmuller, *Phys.Lett.* **B112**, 479 (1982).
- [62] P. Rubin et al. (CLEO Collaboration), *Phys.Rev.* **D72**, 092004 (2005), hep-ex/0508037.
- [63] S. Dobbs et al. (CLEO Collaboration), *Phys.Rev.Lett.* **101**, 182003 (2008), 0805.4599.
- [64] T. Burns, *Phys.Rev.* **D84**, 034021 (2011), 1105.2533.
- [65] E. Eichten, K. Gottfried, T. Kinoshita, K. Lane, and T.-M. Yan, *Phys.Rev.Lett.* **36**, 500 (1976).
- [66] E. Eichten, K. Gottfried, T. Kinoshita, K. Lane, and T.-M. Yan, *Phys.Rev.* **D17**, 3090 (1978).
- [67] T. Barnes and G. Ghandour, *Phys.Lett.* **B118**, 411 (1982).
- [68] D. Ebert, R. Faustov, and V. Galkin, *Mod.Phys.Lett.* **A20**, 875 (2005), hep-ph/0503012.
- [69] E. Eichten, K. Gottfried, T. Kinoshita, K. Lane, and T.-M. Yan, *Phys.Rev.* **D21**, 203 (1980).
- [70] E. S. Swanson, *Phys.Rept.* **429**, 243 (2006), hep-ph/0601110.
- [71] J. Rosner et al. (CLEO Collaboration), *Phys.Rev.Lett.* **95**, 102003 (2005), hep-ex/0505073.
- [72] S. Choi et al. (BELLE collaboration), *Phys.Rev.Lett.* **89**, 102001 (2002), hep-ex/0206002.
- [73] A. Vinokurova et al. (Belle collaboration), *Phys.Lett.* **B706**, 139 (2011), 1105.0978.
- [74] P. del Amo Sanchez et al. (BABAR Collaboration), *Phys.Rev.* **D84**, 012004 (2011), 1103.3971.
- [75] B. Aubert et al. (BABAR Collaboration), *Phys.Rev.Lett.* **92**, 142002 (2004), hep-ex/0311038.
- [76] B. Charron (HAL QCD), *PoS LATTICE2013*, 223 (2014), 1312.1032.
- [77] A. Badalian, B. Bakker, and I. Danilkin, *Phys.Atom.Nucl.* **72**, 638 (2009), 0805.2291.
- [78] K. Murano (HALQCD Collaboration), *PoS LATTICE2011*, 319 (2011), 1112.2051.
- [79] C. Michael, *Nucl.Phys.* **B259**, 58 (1985).
- [80] M. Luscher and U. Wolff, *Nucl.Phys.* **B339**, 222 (1990).
- [81] T. Kawanai and S. Sasaki, in progress.
- [82] S. Aoki et al. (PACS-CS Collaboration), *Phys.Rev.* **D81**, 074503 (2010), 0911.2561.
- [83] S. Sasaki and T. Yamazaki, *Phys.Rev.* **D74**, 114507 (2006), hep-lat/0610081.
- [84] W. Lucha and F. F. Schoberl, *Mod.Phys.Lett.* **A18**, 2837 (2003), hep-ph/0309341.
- [85] C. Lang, L. Leskovec, D. Mohler, S. Prelovsek, and R. Woloshyn, *Phys.Rev.* **D90**, 034510 (2014), 1403.8103.
- [86] A. Mart'nez Torres, E. Oset, S. Prelovsek, and A. Ramos, *JHEP* **05**, 153 (2015), 1412.1706.
- [87] T. Barnes and E. Swanson, *Phys.Rev.* **C77**, 055206 (2008), 0711.2080.

[88] S. Godfrey and R. Kokoski, Phys.Rev. **D43**, 1679 (1991).

[89] F. Close and E. Swanson, Phys.Rev. **D72**, 094004 (2005),

hep-ph/0505206.